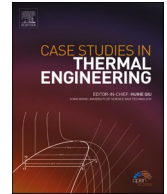


Contents lists available at [ScienceDirect](https://www.sciencedirect.com)

Case Studies in Thermal Engineering

journal homepage: www.elsevier.com/locate/csite

Localized magnetic fields and their effects on heat transfer enhancement and vortices generation in tri-hybrid nanofluids: A novel investigation

Shabbir Ahmad^{a,b,*}, Kashif Ali^b, Assad Ayub^{c,d}, Umaima Bashir^b, Farhan Lafta Rashid^e, Yashar Aryanfar^{f,g}, Mohamed R. Ali^{h,l,**}, Ahmed S. Hendyⁱ, Ismail Shah^j, Liaqat Ali^k

^a Institute of Geophysics and Geomatics, China University of Geosciences, Wuhan, 430074, China

^b Department of Basic Sciences and Humanities, Muhammad Nawaz Sharif University of Engineering and Technology, Multan, 60000, Pakistan

^c Government Post-graduate College Mansehra, Pakistan

^d Department of Mathematics and Statistics, Hazara University, 21300, Pakistan

^e College of Engineering, University of Kerbala, Karbala, Iraq

^f State Key Laboratory of Hydrology-Water Recourses and Hydraulic Engineering, College of Mechanics and Materials, Hohai University, Nanjing, 210098, Jiangsu, China

^g Department of Electric Engineering and Computation, Autonomous University of Ciudad Juárez, Av. Del Charro 450 Norte, Col. Partido Romero, Juárez, Chihuahua, Mexico

^h Faculty of Engineering and Technology, Future University in Egypt New Cairo, 11835, Egypt

ⁱ Department of Computational Mathematics and Computer Science, Institute of Natural Sciences and Mathematics, Ural Federal University, 19 Mira St., Yekaterinburg, 620002, Russia

^j School of Earth Sciences, China University of Geosciences (Wuhan), China

^k School of Sciences, Xi'an Technological University, Xi'an, 710021, China

^l Basic Engineering Science Department, Benha Faculty of Engineering, Benha University, Benha, Egypt

ARTICLE INFO

Handling Editor: Huihe Qiu

Keywords:

Reynolds number

Tri-hybrid nanofluids

Single-phase model

Localized magnetic field

ABSTRACT

A localized magnetic field is a vector field that alters in space because of magnetic materials or electric currents. Some examples of localized magnetic fields are indoor localization, magnetic anomaly detection, magnetoencephalography, and quantum physics. Magnetic fields can be used to estimate the orientation and position of a device inside a building by measuring the changes in the magnetic field caused by ferromagnetic substances. On the other hand, a Tri-hybrid nanofluid can transfer heat better than a normal hybrid nanofluid by mixing three different nanoparticles with synergistic effects. It can have more varied physical and thermal properties by choosing different combinations of nanoparticles. That's why it has more possible uses in various fields such as solar thermal, biomedical, and industrial processes. Therefore, the goal of this research is to explore the complex dynamics of the localized magnetized force that affects the rotation of nanostructures and the vortex formation in the tri-hybrid nanofluid flow regime using the single-phase model, while the governing partial differential equations are discretized numerically. With the help of our self-developed computer codes in MATLAB language, we intend to understand the way these parameters affect the flow and thermal properties of the nanofluids. Additionally, the current work provides a novel analysis that makes it possible to investigate the flow lines and

* Corresponding author. Institute of Geophysics and Geomatics, China University of Geosciences, Wuhan, 430074, China.

** Corresponding author.

E-mail addresses: shabbiraleem@cug.edu.cn (S. Ahmad), mohamed.reda@fue.edu.eg (M.R. Ali).

<https://doi.org/10.1016/j.csite.2023.103408>

Received 16 June 2023; Received in revised form 5 August 2023; Accepted 20 August 2023

Available online 25 August 2023

2214-157X/© 2023 The Authors. Published by Elsevier Ltd. This is an open access article under the CC BY-NC-ND license (<http://creativecommons.org/licenses/by-nc-nd/4.0/>).

isotherms associated with the magnetic strips inside a flow field. It is discovered that the spinning of tri-hybrid nano-particles, which creates the intricate structure of vortices inside the flow regime, results from the magnetized field. Further, the investigations reveal that both the local skin friction (CfRe) and the Nusselt number (Nu) increased by up to 46% and 99% when the magnetic field is strengthened. Finally, adding more nanosized particles in the flow field result in increased both Nu and CfRe, but differently for different nanoparticles. Silver (Ag) had the highest increase in both Nu (55%) and CfRe (110%), showing strong thermal-fluid coupling. Alumina Al_2O_3 and Titanium Dioxide (TiO_2) had lower increases in both Nu (33% and 25%) and CfRe (13% and 9%), showing weaker coupling in the flow regime.

1. Introduction

Vortices are fascinating for every scientist (as they appear) when studying any flow problem because they help to understand how fluids mix and transport mass. The study of vortex generation in lid-driven cavities by localized magnetic is important for learning the fluid dynamics of biological fluids under strong magnetic fields and its medical uses, such as separating cells, targeting drugs, and tracing magnets [1]. It is also important for finding out the effects of fluid flow at small scales, which can matter for liquid crystals, lubricants, and MEMS devices [2]. Moreover, it can reveal the shape and stability of corner vortices in cavity flow, which is a useful problem for testing numerical methods and exploring basic features of incompressible flows in limited volumes [3].

The demand for cooling for industrial systems has led to the development of alternative heat transfer fluids besides traditional ones. Recently, nanofluids have been studied in this context [4–7]. Nanofluids are alternative fluids made by adding nanoparticles smaller than 100 nm to a base fluid, first discovered by Choi in 1995 [8]. Nanofluids have higher thermal conductivity and stability than the base fluid, and lower specific heat, which makes them better heat transfer fluids. Nanofluids have been used in many areas such as heat exchangers, solar collectors, industrial systems, and nuclear systems because of their superior heat transfer performance. Kumar et al. [9] studied how heat and fluid flow in a wavy channel with changing amplitude at the entrance for steady two-dimensional nanofluid flow. They used the finite element method to solve the equations for laminar Cu-water nanofluid flow. They changed the dimensionless length of the varying amplitude section (EL), nanoparticle volume fraction (Φ), and Reynolds number (Re). The wavy channel has a higher heat transfer rate than a plane channel after a critical Re (Recrit) that depends on EL; the heat transfer rate drops with EL. The heat transfer rate rises with ϕ for all EL. The performance factor (PF) shows the combined effects of the higher heat transfer and pressure drop in the wavy channel versus the plane channel. Dey et al. [10] examined the heat and fluid flow in wavy channels of raccoon and serpentine shapes for a laminar viscoplastic fluid. They changed the power-law index (n), Bingham number (Bn), Reynolds number (Re), wave number, and amplitude in realistic ranges and found that the recirculatory zone shrinks with the Bingham number and vanishes at a higher Bingham number. The yielded-unyielded region depends on the shape and Bn range. The wavy channel is better only at a lower Bingham number below a critical limit while the performance factor depends on the rheology and geometry. Mehta & Pati [11] explored the heat, fluid, and entropy flow in an asymmetric wavy channel for MHD nanofluid flow. They used the Galerkin finite element method to solve the equations with the boundary conditions. They changed Hartmann number (Ha), Reynolds number (Re), and nano-particle volume fraction (ϕ). The recirculation zones and vortices in the wavy passages depend on the magnetic field. The heat transfer rate rises with Ha for all ϕ at low and high Reynolds numbers, more for low Reynolds numbers and nanofluids than base fluid, but not at mid-Re. The PFmagnetic drops with Ha at different rates with Reynolds number. The nano-particle increases entropy at a low Reynolds number but decreases it at a high Reynolds number.

Trihybrid nanofluids are a special kind of nanofluids that have three different kinds of nanoparticles mixed in a base fluid. The nanoparticles can be made of metals, metal oxides, or carbon-based materials. These nanofluids can have better thermal and physical properties than ordinary nanofluids. Trihybrid nanofluids have many possible uses in different fields, such as heat transfer, energy storage systems, electronic cooling, and biomedical engineering. Researchers are exploring the behavior and potential applications of nanofluids. They want to improve their performance and find new ways to use them in various domains. Jayakumar et al. [12] studied the thermal dissipation efficacy of bracket housing using aqueous solutions and different nanofluids. They found that Ga-In-Sn nanofluids outperformed alternative nanofluids and water in improving heat transfer efficiency, reducing operational temperature, and showcasing their potential for enhancing electric vehicles. Biswas et al. [13] showed the effect of partial magnetic fields on the heat transfer of hybrid nanofluid flow in a slanted wavy porous enclosure. The bottom is partially heated, the wavy sides are cooled, and the sidewalls have a partial magnetic field normal to them. They solved the equations with complex wavy walls, local thermal gradient, porous substance, partial magnetic fields, and hybrid nanofluid by the finite volume approach with a FORTRAN code. They tested the partial magnetic field for active magnetic widths (Wb), different active heating lengths (Lh), and positions, cavity inclination (γ), magnetic strength (Ha), Darcy number (Da), Darcy-Rayleigh number (Ram), and hybrid nanoparticles concentration (ζ) with no and whole-domain magnetic field. They found that the wavy walls increase the heat transfer by $\sim 22.16\%$ than a plain wall, but decrease the circulation. A partial magnetic field can control the field variables with less heat transfer reduction ($\sim 13.97\%$) than the whole domain magnetic field. The middle-centered partial magnetic field affects the thermal behavior depending on the intensity, magnetic width, heating length, and other parameters. Mehta & Pati [14] studied the heat and fluid flow in a channel with a wavy top

wall and a flat bottom wall with metal porous blocks. They used COMSOL Multiphysics® and a finite element method to solve the equations. The porous blocks affect the heat transfer rate, and the local Nusselt number rises with the Darcy number. The average Nusselt number drops with Darcy's number for the top wall and increases for the bottom wall. The average Nusselt number for wavy channels with porous blocks (WCPB) is much higher than for wavy channels without porous blocks (WCWPB). The effects of localized magnetic forces on a tri-hybrid nanofluid flow regime were investigated by Ahmad et al. [15]. When tri-hybrid nanoparticles were subjected to a magnetic field, their rotational mobility was drastically altered. Rajesh et al. [16] studied natural convection in an enclosure using ternary hybrid nanofluids. The study examined how nanomaterial composition and non-uniform heating affect the energy transfer in the enclosure, where a nanomaterial enhances energy transfer and heat conduction decreases due to the lower thermal energy of the heated wall.

Al_2O_3 - TiO_2 -based dielectric ceramics [17], $\text{Al}_2\text{O}_3/\text{TiO}_2/\text{TiN}$ nanotubes [18], and $\text{Ag-TiO}_2/\gamma\text{-Al}_2\text{O}_3/\text{Chitosan}$ nano compound photocatalyst [19] are some examples of nanomaterials that can exhibit novel features for various applications. Dielectric ceramics can offer high thermal conductivity and temperature stability, which are essential for low-temperature co-fired ceramics (LTCC) applications that require high performance and reliability. The nanotubes can convert light energy into heat energy with high efficiency, which makes them suitable for photodetector applications that need a fast and sensitive response. The nano-composite photocatalyst can improve the nitrate reduction by photocatalysis in water by combining the benefits of coupling and Ag-doping with $\gamma\text{-Al}_2\text{O}_3$ nanoparticles, which enhances the light absorption and charge separation of the catalyst. Ag can be used as a sintering additive for Al_2O_3 - TiO_2 -based dielectric ceramics to achieve low-temperature co-firing and strong thermal conductivity [20]. It can be employed as a plasmonic material for enhancing the surface-enhanced Raman scattering (SERS) signals of nanostructures and also serve as a substrate for Au deposition involving simultaneous reduction reactions and galvanic replacement [21]. Khan et al. discussed three different topics of nanomaterials. First, it examines the synthesis and characteristics of graphene-based metal and metal oxide nanocomposites, which have a wide range of applications. Second, it describes the environmentally friendly and cost-effective green synthesis of silver nanoparticles utilizing *Pulicaria glutinosa* extract. Third, it describes the biogenic synthesis of palladium nanoparticles using the same extract, as well as their catalytic activity for the Suzuki coupling reaction, which is a common organic synthesis method [22–24].

Its importance is evident in many systems that rely on improved thermal performance, as it helps them achieve lower costs, higher efficiency, and better environmental outcomes. These flows are also eminent in heating and cooling energy systems. Examples of cavity flows incorporate solar collectors, boilers, underground water flow, nuclear reactors, and so on. Natural convection flow problems are mainly concerned with a heat transfer performance of a working fluid. At the beginning of the 21st century, scientists started working on the improvement of fluid's thermal conductivities by the accumulation of tiny-sized nanocrystalline particles in carrier fluids [8,25,26]. Mandal et al. [27] investigated the heat and fluid flow in a partially driven cavity (PDC) with Cu-water nano liquid, and porous substance under a magnetic field. The upper half of the vertical walls are cooled and slid, and the bottom wall is heated. They explored MHD convection in a nano-liquid porous system. The parameters involved are thermal buoyancy, cavity orientation, magnetic intensity, porous permeability, and nanoparticle suspension. They used a finite volume-based code to solve the equations. They used staggered nonuniform grids and the SIMPLE algorithm technique with a convergence check. The study showed that the heat transfer increases with Richardson (Ri) and Reynolds numbers (Re), regardless of the porous substance, magnetic field, or nanofluid concentration. The wall motions affect the flow vortices and heat transfer while the cavity orientation changes with the transport process. The upward wall velocity for both sidewalls enhances the heat transfer (about 88.39% at $\text{Ri} = 0.1$ and $\text{Re} = 200$). Several practical applications related to microelectronics, cooling and heating systems of buildings, and insulations have been projected in the investigations of Heindel et al. [28–31], Sankar et al. [32], Muftuoglu and Bilgen [33], Nardini and Paroncini [34], and Saglam et al. [35]. In these investigations, it is observed that the dimension and location of the heat sources in the enclosures are of substantial importance. Again, Mandal et al. [36] considered MHD mixed bioconvection with oxytactic microorganisms in copper-water nanofluid. The flow goes through porous media in a moving enclosure with a wavy heated sidewall. The right wall is cooled, other walls are adiabatic. A horizontal magnetic field is applied. They modeled this problem with an undulating heated wall and many coupled equations (due to the bacteria) and solved them with a finite volume-based code. They analyzed the thermo-fluid behaviors to explore the effects of different parameters that could help the system. The parameters are the undulations (n), Darcy number (Da), bioconvection Rayleigh number (Rb), Hartmann number (Ha), Lewis number (Le), Peclet number (Pe), Grashof number (Gr), oxygen diffusion ratio (γ). The study revealed that the curved surface increases the heat transfer until some optimal undulations at different conditions. The mass transfer rate rises with all undulations and bioconvection. Bioconvection helps heat transfer. They found that by changing the parameters and undulations, local and global transport can be controlled well.

There is a lack of studies on the vortex generation of tri-hybrid nanofluids in lid-driven cavities under the influence of localized magnetic fields. This is the research gap that motivates the present study. The objectives of this study are:

- To investigate the effects of localized magnetic fields on the fluid flow and heat transfer characteristics of tri-hybrid nanofluids in lid-driven cavities.
- To analyze the effects of various parameters, such as Reynolds number, Nusselt number, etc., on the vortex generation and heat transfer enhancement of tri-hybrid nanofluids in a lid-driven cavity under localized magnetic fields.

In this paper, we investigate the vortex generation and heat transfer enhancement of Ag-Al₂O₃-TiO₂-water based tri-hybrid nanofluids in a lid-driven cavity under localized magnetic fields. This is a novel and important research topic that has not been addressed adequately in the literature. The main contributions and novelties of this paper are:

- We developed a numerical method based on the 4. Alternating Direction Implicit (ADI) technique to solve the governing equations of tri-hybrid nanofluids flow and heat transfer under localized magnetic fields. This method is efficient, accurate, and stable for solving complex problems involving multiple nanoparticles and magnetic field localization. We analyzed and discussed the effects of various parameters, such as Reynolds number, volume fraction, and magnetic field intensity.
- We provided physical insights and explanations for the observed phenomena, such as the spinning of nanoparticles, the formation and removal of vortices, the enhancement of local skin friction and Nusselt number, and the thermal-fluid coupling in the flow.

2. Problem description

As shown in Fig. 1, this study takes into account a schematic illustration of a 2-dimensional lid-driven cavity with a side length of L . A confined magnetic field has been incorporated constantly in the bottom wall of the enclosure. In order to describe the fluid flow and heat transfer developments inside the cavity, a single-phase model (SPM) is implemented to formulate the fundamental equations of mass, momentum, and energy conservation in a two-dimensional Cartesian coordinate system.

2.1. Basic assumptions

The study is conducted under the following fundamental assumptions.

A magnetic source produces a magnetic field with intensity H , as determined by the equation:

$\tilde{H}_1(x,y) = H_0\{\tanh A'_1(x - x_1) - \tanh A'_2(x - x_2)\}$, $\tilde{H}_2(x,y) = H_0\{\tanh A'_1(x - x_3) - \tanh A'_2(x - x_4)\}$, $\tilde{H}_3(x,y) = H_0\{\tanh A'_1(y - y_1) - \tanh A'_2(y - y_2)\}$, $\tilde{H}_4(x,y) = H_0\{\tanh A'_1(y - y_3) - \tanh A'_2(y - y_4)\}$, in the strips mentioned by $x_1 \leq x \leq x_2, x_3 \leq x \leq x_4; 0 \leq y \leq L$ and $y_1 \leq y \leq y_2, y_3 \leq y \leq y_4; 0 \leq x \leq L$ respectively. A square cavity consists of vertical walls which are insulated and horizontal walls have a fixed temperature. Both upper and lower horizontal walls move from the -ve x-axis with the same velocity. The tri-hybrid nanofluids have Newtonian, incompressible, and laminar properties, and they are created through the interaction of solid nanoparticles containing Ag, Al₂O₃, and TiO₂ nanostructures and considering water as a base fluid that is in thermal equilibrium. The thermophysical properties of the nanofluid, such as density, thermal conductivity, viscosity, and specific heat, are constant.

3. Mathematical formulation

The basic laws, assumptions, and derivation of the Navier-Stokes Equations (NSE) are based on the following principles:

- The fluid is a continuum, i.e., it may be handled more like a continuous material than a collection of distinct particles.
- The fluid is incompressible, i.e. its density is constant and independent of pressure [37].
- The fluid is Newtonian, i.e. its stress is proportional to its strain rate[37].
- The fluid obeys the conservation of mass, i.e., the mass of a fluid element does not change as it moves.
- The fluid obeys the conservation of momentum, i.e., the net force acting on a fluid is equal to its rate of change of momentum.
- The fluid obeys the conservation of energy, i.e., the net work done on a fluid element is equal to its rate of change of energy

These equations have the following dimensional form [38]:

Continuity equation:

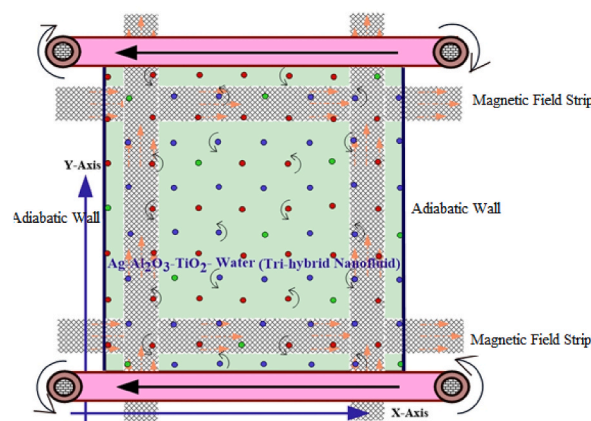


Fig. 1. Physical diagram of the problem with straight arrows indicating the region of localization of magnetic field.

$$\frac{\partial \tilde{U}}{\partial x} + \frac{\partial \tilde{V}}{\partial y} = 0, \tag{1}$$

Momentum equation:

$$\frac{\partial \tilde{U}}{\partial t} + \left(\tilde{V} \frac{\partial \tilde{U}}{\partial y} + \tilde{U} \frac{\partial \tilde{U}}{\partial x} \right) = -\frac{1}{\rho_{hnf}} \frac{\partial P}{\partial x} + \hat{v}_{hnf} \left(\frac{\partial^2 \tilde{U}}{\partial y^2} + \frac{\partial^2 \tilde{U}}{\partial x^2} \right) + \frac{\bar{\mu}_o \tilde{M}}{\rho_{hnf}} \frac{\partial \tilde{H}}{\partial x}, \tag{2}$$

$$\frac{\partial \tilde{V}}{\partial t} + \left(\tilde{U} \frac{\partial \tilde{V}}{\partial x} + \tilde{V} \frac{\partial \tilde{V}}{\partial y} \right) = -\frac{1}{\rho_{hnf}} \frac{\partial P}{\partial y} + \hat{v}_{hnf} \left(\frac{\partial^2 \tilde{V}}{\partial x^2} + \frac{\partial^2 \tilde{V}}{\partial y^2} \right) + \frac{\bar{\mu}_o \tilde{M}}{\rho_{hnf}} \frac{\partial \tilde{H}}{\partial y}, \tag{3}$$

Energy Equation:

$$\frac{(\rho c_p)_{hnf}}{k_{hnf}} \left(\tilde{U} \frac{\partial T}{\partial x} + \tilde{V} \frac{\partial T}{\partial y} \right) + \left(\frac{\bar{\mu}_o}{k_{hnf}} \right) T \frac{\partial \tilde{M}}{\partial T} \left(\tilde{V} \frac{\partial \tilde{H}}{\partial y} + \tilde{U} \frac{\partial \tilde{H}}{\partial x} \right) = \nabla^2 T + \left(\frac{\bar{\mu}_{hnf}}{k_{hnf}} \right) \left\{ 2 \left(\frac{\partial \tilde{U}}{\partial x} \right)^2 + \left(\frac{\partial \tilde{V}}{\partial x} + \frac{\partial \tilde{U}}{\partial y} \right)^2 + 2 \left(\frac{\partial \tilde{V}}{\partial y} \right)^2 \right\}. \tag{4}$$

Here:

$\bar{\mu}_o \tilde{M} \frac{\partial \tilde{H}}{\partial x}$ the X-axis magnetic force components $\bar{\mu}_o \tilde{M} \frac{\partial \tilde{H}}{\partial y}$ the Y-axis magnetic force components

$\bar{\mu}_o T \frac{\partial \tilde{M}}{\partial T} \left(\tilde{U} \frac{\partial \tilde{H}}{\partial x} + \tilde{V} \frac{\partial \tilde{H}}{\partial y} \right)$ magneto-caloric phenomenon γ magnetic field strength

$\tilde{M} = K\tilde{H}(\bar{T}_c - T)$, magnetization property \bar{T}_c Curie temperature [39]

$\frac{\partial \tilde{U}}{\partial t} + \left(\tilde{V} \frac{\partial \tilde{U}}{\partial y} + \tilde{U} \frac{\partial \tilde{U}}{\partial x} \right)$ Convection terms $\left(\frac{\partial^2 \tilde{U}}{\partial y^2} + \frac{\partial^2 \tilde{U}}{\partial x^2} \right)$ Diffusion terms

$\frac{\partial \tilde{V}}{\partial t} + \left(\tilde{U} \frac{\partial \tilde{V}}{\partial x} + \tilde{V} \frac{\partial \tilde{V}}{\partial y} \right)$ Convection terms $\left(\frac{\partial^2 \tilde{V}}{\partial y^2} + \frac{\partial^2 \tilde{V}}{\partial x^2} \right)$ Diffusion terms

Eliminating the pressure term results in:

$$\begin{aligned} & \frac{\partial}{\partial t} \left(\frac{\partial \tilde{U}}{\partial y} - \frac{\partial \tilde{V}}{\partial x} \right) + \tilde{V} \frac{\partial}{\partial y} \left(\frac{\partial \tilde{U}}{\partial y} - \frac{\partial \tilde{V}}{\partial x} \right) + \tilde{U} \frac{\partial}{\partial x} \left(\frac{\partial \tilde{U}}{\partial y} - \frac{\partial \tilde{V}}{\partial x} \right) \\ & = \hat{v}_{hnf} \left(\frac{\partial^2}{\partial x^2} + \frac{\partial^2}{\partial y^2} \right) \left(\frac{\partial \tilde{U}}{\partial y} - \frac{\partial \tilde{V}}{\partial x} \right) + \left(\frac{\partial \left(\frac{\bar{\mu}_o \tilde{M}}{\rho_{hnf}} \frac{\partial \tilde{H}}{\partial x} \right)}{\partial y} - \frac{\partial \left(\frac{\bar{\mu}_o \tilde{M}}{\rho_{hnf}} \frac{\partial \tilde{H}}{\partial y} \right)}{\partial x} \right). \end{aligned} \tag{5}$$

3.1. Boundary conditions

The following are the dimensions boundary conditions for the current obstacle:

Left and Right Vertical Walls (Adiabatic): The heat flux across these walls is zero, i.e.,

$$\tilde{U}(0, y) = \tilde{U}(L, y) = 0, \left(\frac{\partial T}{\partial x} \right)_{x=0} = \left(\frac{\partial T}{\partial x} \right)_{x=L} = 0, \tilde{V}(0, y) = \tilde{V}(L, y) = 0; \quad 0 < y < L \tag{6a}$$

Upper Horizontal Wall:

$$\tilde{U}(x, L) = -V_0, T(x, L) = T_c, \tilde{V}(x, L) = 0; \quad 0 < x < L \tag{6b}$$

Lower Horizontal Wall:

$$\tilde{U}(x, 0) = -V_0, T(x, 0) = T_h, \tilde{V}(x, 0) = 0; \quad 0 < x < L. \tag{6c}$$

3.2. The characteristics of tri hybrid nanofluids (Ag- Al₂O₃-TiO₂)

In this section, the thermo-physical features of the tri-hybrid nanofluids used in this analysis are presented. The thermo-physical characteristics of the tri-hybrid nanofluids are the backbone for the investigation of the heat transport problem. We consider a certain

combination of thermo-physical properties for the tri-hybrid nanofluids composed of Ag- Al₂O₃-TiO₂ nanoparticles. These thermo-physical parameters include the density, specific heat, thermal conductivity, and viscosity of the tri-hybrid nanofluids, and they are obtained and confirmed from the existing literature [40–48]. Each symbol in Table 1 is explained in Table 1.

	For Tri-hybrid nanofluids	For Hybrid nanofluids	For nanofluids	For base fluids (water)	For solid		
					Silver (s ₁)	Aluminium oxide (s ₂)	Titanium dioxide (s ₃)
Thermal conductivity	k_{thnf}	k_{hnf}	k_{nf}	k_f	k_{s1}	k_{s2}	k_{s3}
Density	$\hat{\rho}_{thnf}$			$\hat{\rho}_f$	$\hat{\rho}_{s1}$	$\hat{\rho}_{s2}$	$\hat{\rho}_{s3}$
Electrical conductivity	σ_{thnf}	σ_{hnf}	σ_{nf}	σ_f	σ_{s1}	σ_{s2}	σ_{s3}
Viscosity	μ_{thnf}	μ_{hnf}	μ_{nf}	μ_f			
Nanoparticles volume fraction					$\hat{\varphi}_1$	$\hat{\varphi}_2$	$\hat{\varphi}_3$

The thermophysical features of a tri-hybrid nanofluid could be evaluated by considering the models proposed in the literature. The following set of dimensionless variables should be used right now:

$$\xi = \frac{x}{L}, y = \frac{y}{L}, u = \frac{\tilde{U}}{V_0}, v = \frac{\tilde{V}}{V_0}, \hat{\theta} = \frac{T - T_c}{\Delta T}, H = \frac{\tilde{H}}{H_0}, t = \frac{V_0 t'}{L} \tag{7}$$

From equations (4) and (5), we can deduce that;

$$\frac{\partial J}{\partial t} + u \frac{\partial J}{\partial \xi} + v \frac{\partial J}{\partial \eta} = (1 - \hat{\varphi}_1) \left(1 - \hat{\varphi}_2 + \hat{\varphi}_3 \left(\hat{\rho}_{s1} / \hat{\rho}_f \right) + \hat{\varphi}_2 \left(\hat{\rho}_{s2} / \hat{\rho}_f \right) \right) (1 - \hat{\varphi}_2)^{2.5} (1 - \hat{\varphi}_3)^{2.5} \frac{1}{\text{Re}} \nabla^2 J + \frac{Mn}{(1 - \hat{\varphi}_2) \left(1 - \hat{\varphi}_1 + \hat{\varphi}_2 \left(\hat{\rho}_{s1} / \hat{\rho}_f \right) + \hat{\varphi}_3 \left(\hat{\rho}_{s2} / \hat{\rho}_f \right) \right)} H \left(\frac{\partial H}{\partial \eta} \frac{\partial \hat{\theta}}{\partial \xi} - \frac{\partial H}{\partial \xi} \frac{\partial \hat{\theta}}{\partial \eta} \right), \tag{8}$$

Table 1
Thermophysical attributes of tri-hybrid and conventional nanofluids.

Properties	Tri-hybrid nanofluid(thnf)
Density	$\hat{\rho}_{thnf} = (1 - \hat{\varphi}_3) \{ (1 - \hat{\varphi}_1) \{ (1 - \hat{\varphi}_2) \hat{\rho}_f + \hat{\varphi}_1 \hat{\rho}_{s1} \} + \hat{\varphi}_2 \hat{\rho}_{s2} \} + \hat{\varphi}_3 \hat{\rho}_{s3}$
Heat capacity	$(\hat{\rho} c_p)_{thnf} = (1 - \hat{\varphi}_3) \{ (1 - \hat{\varphi}_2) \{ (1 - \hat{\varphi}_1) \hat{\rho}_f + \hat{\varphi}_1 \hat{\rho}_{s1} \} + \hat{\varphi}_2 \hat{\rho}_{s2} \} + \hat{\varphi}_3 \hat{\rho}_{s3}$
viscosity	$\mu_{thnf} = \frac{\mu_f}{(1 - \hat{\varphi}_1)^{2.5} (1 - \hat{\varphi}_2)^{2.5} (1 - \hat{\varphi}_3)^{2.5}}$
Thermal conductivity	$\frac{k_{thnf}}{k_{nf}} = \frac{k_{s3} + (n - 1)(k_{hnf} - (n - 1)\hat{\varphi}_{s3})(k_{hnf} - k_{s3})}{k_{s3} + (n - 1)k_{hnf} + \hat{\varphi}_{s3}(k_{hnf} - k_{s3})}$
	where $\frac{k_{thnf}}{k_{nf}} = \frac{k_{s2} - (n - 1)\hat{\varphi}_2(k_{nf} - k_{s3}) + (n - 1)k_{nf}}{k_{s2} + \hat{\varphi}_2(k_{nf} - k_{s3}) + (n - 1)k_{nf}}$
	and $\frac{k_{nf}}{k_f} = \frac{k_{s1} - (n - 1)\hat{\varphi}_1(k_f - k_{s1}) + (n - 1)k_f}{k_{s1} + \hat{\varphi}_1(k_f - k_{s1}) + (n - 1)k_f}$
Electric conductivity	$\frac{\sigma_{thnf}}{\sigma_{nf}} = \frac{\sigma_{s3} - 2\hat{\varphi}_3(\sigma_{nf} - \sigma_{s3}) + 2\sigma_{nf}}{\sigma_{s3} + \hat{\varphi}_3(\sigma_{nf} - \sigma_{s3}) + 2\sigma_{nf}}$
	where $\frac{\sigma_{thnf}}{\sigma_{nf}} = \frac{\sigma_{s2} - 2\hat{\varphi}_2(\sigma_{nf} - \sigma_{s2}) + 2\sigma_{nf}}{\sigma_{s2} + \hat{\varphi}_2(\sigma_{nf} - \sigma_{s2}) + 2\sigma_{nf}}$
	and $\frac{\sigma_{nf}}{\sigma_f} = \frac{\sigma_{s1} - 2\hat{\varphi}_1(\sigma_f - \sigma_{s1}) + 2\sigma_f}{\sigma_{s1} + \hat{\varphi}_1(\sigma_f - \sigma_{s1}) + 2\sigma_f}$

$$\begin{aligned}
 \nabla^2 \hat{\theta} = & \Pr * \left(\frac{\left((1 - \hat{\varphi}_2) \left(1 - \hat{\varphi}_1 + \hat{\varphi}_2 \left(\hat{\rho} s_1 / \hat{\rho}_f \right) + \hat{\varphi}_3 \left(\hat{\rho} s_2 / \hat{\rho}_f \right) \right) \right)}{\left(1 - \hat{\varphi}_1 \right)^{-2.5} \left(1 - \hat{\varphi}_2 \right)^{-2.5}} \right) * \left(1 - \hat{\varphi}_2 \right) \left(1 - \hat{\varphi}_1 + \hat{\varphi}_2 \left(\hat{\rho} s_1 * c_{p s_1} / \hat{\rho}_f * c_{p f} \right) \right) \\
 & + \hat{\varphi}_3 \left(\hat{\rho} s_3 * c_{p s_3} / \hat{\rho}_f * c_{p f} \right) \\
 \text{Re} * & \left(\frac{\left(1 - \hat{\varphi}_1 \right)^{-2.5} \left(1 - \hat{\varphi}_2 \right)^{-2.5}}{\left(1 - \hat{\varphi}_2 \right) \left(1 - \hat{\varphi}_1 + \hat{\varphi}_2 \left(\hat{\rho} s_1 / \hat{\rho}_f \right) + \hat{\varphi}_3 \left(\hat{\rho} s_3 / \hat{\rho}_f \right) \right)} \right) \left\{ \frac{\partial \hat{\theta}}{\partial \xi} \frac{\partial \tilde{\psi}}{\partial \eta} - \frac{\partial \hat{\theta}}{\partial \eta} \frac{\partial \tilde{\psi}}{\partial \xi} \right\} \\
 & + \Pr * \left(\frac{\left((1 - \hat{\varphi}_2) \left(1 - \hat{\varphi}_1 + \hat{\varphi}_2 \left(\hat{\rho} s_1 / \hat{\rho}_f \right) + \hat{\varphi}_3 \left(\hat{\rho} s_2 / \hat{\rho}_f \right) \right) \right)}{\left(1 - \hat{\varphi}_1 \right)^{-2.5} \left(1 - \hat{\varphi}_2 \right)^{-2.5}} \right) \\
 & * \left(1 - \hat{\varphi}_2 \right) \left(1 - \hat{\varphi}_1 + \hat{\varphi}_1 \left(\hat{\rho} s_1 * c_{p s_1} / \hat{\rho}_f * c_{p f} \right) + \hat{\varphi}_2 \left(\hat{\rho} s_2 * c_{p s_2} / \hat{\rho}_f * c_{p f} \right) \right) \\
 & * \frac{Mn}{\left(1 - \hat{\varphi}_2 \right) \left(1 - \hat{\varphi}_1 + \hat{\varphi}_1 \left(\hat{\rho} s_1 / \hat{\rho}_f \right) + \hat{\varphi}_2 \left(\hat{\rho} s_2 / \hat{\rho}_f \right) \right)} \\
 \text{Re} * & \left(\frac{\left(1 - \hat{\varphi}_1 \right)^{-2.5} \left(1 - \hat{\varphi}_3 \right)^{-2.5}}{\left(1 - \hat{\varphi}_2 \right) \left(1 - \hat{\varphi}_1 + \hat{\varphi}_1 \left(\hat{\rho} s_1 / \hat{\rho}_f \right) + \hat{\varphi}_3 \left(\hat{\rho} s_3 / \hat{\rho}_f \right) \right)} \right) EcH(e - \tilde{\psi}) \left\{ \frac{\partial H}{\partial \xi} \frac{\partial \tilde{\psi}}{\partial \eta} - \frac{\partial H}{\partial \eta} \frac{\partial \tilde{\psi}}{\partial \xi} \right\} \\
 & + \Pr * \left(\frac{\left((1 - \hat{\varphi}_2) \left(1 - \hat{\varphi}_1 + \hat{\varphi}_1 \left(\hat{\rho} s_1 / \hat{\rho}_f \right) + \hat{\varphi}_3 \left(\hat{\rho} s_2 / \hat{\rho}_f \right) \right) \right)}{\left(1 - \hat{\varphi}_1 \right)^{-2.5} \left(1 - \hat{\varphi}_2 \right)^{-2.5}} \right) \\
 & * \left(1 - \hat{\varphi}_2 \right) \left(1 - \hat{\varphi}_1 + \hat{\varphi}_1 \left(\hat{\rho} s_1 * c_{p s_1} / \hat{\rho}_f * c_{p f} \right) + \hat{\varphi}_2 \left(\hat{\rho} s_2 * c_{p s_2} / \hat{\rho}_f * c_{p f} \right) \right) Ec \left\{ \left(\frac{\partial^2 \tilde{\psi}}{\partial \eta^2} - \frac{\partial^2 \tilde{\psi}}{\partial \xi^2} \right)^2 + 4 \left(\frac{\partial^2 \tilde{\psi}}{\partial \xi \partial \eta} \right)^2 \right\},
 \end{aligned} \tag{9a}$$

Where,

$$\begin{aligned}
 H_1(\xi, \eta) &= H_0 \{ \tanh A'_1(\xi - \xi_1) - \tanh A'_2(\xi - \xi_2) \}, \\
 H_2(\xi, \eta) &= H_0 \{ \tanh A_1(\xi - \xi_3) - \tanh A_2(\xi - \xi_4) \}, \\
 H_3(\xi, \eta) &= H_0 \{ \tanh A'_1(\eta - \eta_1) - \tanh A'_2(\eta - \eta_2) \}, \\
 H_4(\xi, \eta) &= H_0 \{ \tanh A_1(\eta - \eta_3) - \tanh A_2(\eta - \eta_4) \}
 \end{aligned} \tag{9b}$$

in the strips defined by $\xi_1 \leq \xi \leq \xi_2, \xi_3 \leq \xi \leq \xi_4; 0 \leq \eta \leq 1$ and $\eta_1 \leq \eta \leq \eta_2, \eta_3 \leq \eta \leq \eta_4; 0 \leq \xi \leq 1$, respectively.

$$\text{Finally, } H(\xi, \eta) = H_1(\xi, \eta) + H_2(\xi, \eta) + H_3(\xi, \eta) + H_4(\xi, \eta) \tag{9c}$$

The equations above represent the stream-vorticity formulation, which is a modified version of Equations (1)–(4) with

$$\hat{u} = \frac{\partial \tilde{\psi}}{\partial \eta}, \hat{v} = \frac{\partial \tilde{\psi}}{\partial \xi} \text{ and } \left(\frac{\partial \hat{u}}{\partial \eta} - \frac{\partial \hat{v}}{\partial \xi} \right) = -\hat{\omega} \text{ or } \left\{ \left(\frac{\partial^2 \tilde{\psi}}{\partial \xi^2} + \frac{\partial^2 \tilde{\psi}}{\partial \eta^2} \right) = -\hat{\omega} \right\}. \tag{10}$$

Similarly, the boundary conditions in the dimensionless form are expressed as:

Left and Right Vertical Walls (Adiabatic):

$$\widehat{u}(0, \eta) = \widehat{u}(1, \eta) = 0, \left(\frac{\partial \theta}{\partial \xi}\right)_{\xi=0} = 0, \left(\frac{\partial \theta}{\partial \xi}\right)_{\xi=1} = 0, \widehat{v}(0, \eta) = \widehat{v}(1, \eta) = 0, 0 < \eta < 1 \tag{11a}$$

Upper Horizontal Wall:

$$\widehat{u}(\xi, 1) = -1, \widehat{\theta}(\xi, 1) = 0, \widehat{v}(\xi, 1) = 0; \quad 0 < \xi < 1 \tag{11b}$$

Lower Horizontal Wall:

$$\widehat{u}(\xi, 0) = -1, \widehat{\theta}(\xi, 0) = 1, \widehat{v}(\xi, 0) = 0; \quad 0 < \xi < 1. \tag{11c}$$

3.3. Physical quantities of interest

The primary quantities of interest in this study are the Nusselt number (*Nu*) and the skin friction (*CfRe*), which are defined by:

$$Nu = \frac{\widehat{q} L}{k_{mf} \Delta T} \text{ and } CfRe = \frac{2\tau}{\widehat{\rho}_{mf} v_0^2}$$

where,

$$\tau = \widetilde{\mu}_{mf} \left(\frac{\partial \widehat{u}}{\partial \eta}\right)_{\eta=0,L} \text{ shear stress } \widehat{q} = -k_{mf} \left(\frac{\partial T}{\partial \eta}\right)_{\eta=0,L} \text{ heat flux}$$

Using the dimensionless variables, we get: Using the dimensionless variables, we get:

$$CfRe = 2 \frac{\left[(1 - \widehat{\varphi}_1)(1 - \widehat{\varphi}_2)(1 - \widehat{\varphi}_3) \right]^{2.5}}{\left[(1 - \widehat{\varphi}_3) \left\{ (1 - \widehat{\varphi}_2) \left(1 - \widehat{\varphi}_1 + \widehat{\varphi}_1 \frac{\widehat{\rho}_{s1}}{\widehat{\rho}_f} \right) + \widehat{\varphi}_2 \frac{\widehat{\rho}_{s2}}{\widehat{\rho}_f} \right\} + \widehat{\varphi}_3 \frac{\widehat{\rho}_{s3}}{\widehat{\rho}_f} \right]} \frac{\partial \widehat{u}}{\partial y}, \text{ and } Nu = \frac{k_{mf}}{k_f} \frac{\partial \widehat{\theta}}{\partial y}.$$

4. Alternating Direction Implicit (ADI) technique

A numerical solution of the dimensionless NSE and energy equations (4)–(6) is obtained using an ADI method and central difference schemes for the derivatives. The ADI methodology employs a numerical scheme that alternates the direction of implicitness between the x-direction and the y-direction while holding the other direction explicitly. This enhances the computational efficiency and the stability of the solution. The central difference approximation utilizes the mean values at the adjacent points to estimate the gradient at a given point. This is an effective and precise way to discretize the differential equations on a structured grid. A structured grid is a grid that has a uniform pattern of points and can be readily indexed by row and column numbers. A finite difference method is a universal numerical technique that can be applied to solve differential equations by substituting them with algebraic equations on a grid. Finite differences can also be beneficial in other scenarios when we need to estimate derivatives from discrete data. One of the merits of the finite difference method is that it is straightforward to implement and achieve high-order approximations by using more points in the stencil; a collection of points that are used to calculate the finite difference approximation at a given point.

The scheme for moving from time level *n* to time level (*n*+1) has the following details:

$$\begin{aligned} \frac{\widehat{w}_{ij}^{(n+1/2)} - \widehat{w}_{ij}^{(n)}}{\delta t/2} = Re * & \left(\frac{(1 - \widehat{\varphi}_1)^{-2.5} (1 - \widehat{\varphi}_2)^{-2.5} (1 - \widehat{\varphi}_3)^{-2.5}}{\left((1 - \widehat{\varphi}_3) \left[(1 - \widehat{\varphi}_1) \left\{ (1 - \widehat{\varphi}_2) \widehat{\rho}_f + \widehat{\varphi}_1 \widehat{\rho}_{s1} / \widehat{\rho}_f \right\} + \widehat{\varphi}_2 \widehat{\rho}_{s2} / \widehat{\rho}_f \right] + \widehat{\varphi}_3 \widehat{\rho}_{s3} / \widehat{\rho}_f \right)} \right) \\ & \left\{ \frac{\widehat{w}_{i-1,j}^{(n+1/2)} - 2\widehat{w}_{ij}^{(n+1/2)} + \widehat{w}_{i+1,j}^{(n+1/2)}}{h^2} + \frac{\widehat{w}_{ij,j-1}^{(n)} - 2\widehat{w}_{ij}^{(n)} + \widehat{w}_{ij,j+1}^{(n)}}{k^2} \right\} \\ & + \frac{Mn}{\left((1 - \widehat{\varphi}_3) \left[(1 - \widehat{\varphi}_1) \left\{ (1 - \widehat{\varphi}_2) \widehat{\rho}_f + \widehat{\varphi}_1 \widehat{\rho}_{s1} / \widehat{\rho}_f \right\} + \widehat{\varphi}_2 \widehat{\rho}_{s2} / \widehat{\rho}_f \right] + \widehat{\varphi}_3 \widehat{\rho}_{s3} / \widehat{\rho}_f \right)} \\ H_{i,j} & \left\{ \frac{H_{i,j+1} - H_{i,j-1}}{2k} \frac{\widehat{\theta}_{i+1,j}^{(n)} - \widehat{\theta}_{i-1,j}^{(n)}}{2h} - \frac{H_{i+1,j} - H_{i-1,j}}{2h} \frac{\widehat{\theta}_{i,j+1}^{(n)} - \widehat{\theta}_{i,j-1}^{(n)}}{2k} \right\} \\ -\widehat{u}_{ij}^{(n+1/2)} & \left(\frac{\widehat{w}_{i+1,j}^{(n+1)} - \widehat{w}_{i-1,j}^{(n+1)}}{2h} \right) - \widehat{v}_{ij}^{(n+1/2)} \left(\frac{\widehat{w}_{i,j+1}^{(n)} - \widehat{w}_{i,j-1}^{(n)}}{2k} \right) \end{aligned} \tag{12}$$

$$\begin{aligned}
 \frac{\widehat{\theta}^{(n+1/2)}_{ij} - \widehat{\theta}^{(n)}_{ij}}{\delta t/2} &= \left\{ \frac{\widehat{\theta}^{(n+1/2)}_{i-1j} - 2\widehat{\theta}^{(n+1/2)}_{ij} + \widehat{\theta}^{(n+1/2)}_{i+1j}}{h^2} + \frac{\widehat{\theta}^{(n)}_{ij-1} + \widehat{\theta}^{(n)}_{ij+1} - 2\widehat{\theta}^{(n)}_{ij}}{k^2} \right\} \\
 + \text{Pr} * &\left(\frac{\left(\left((1 - \widehat{\varphi}_3) \left[(1 - \widehat{\varphi}_1) \left\{ (1 - \widehat{\varphi}_2) \widehat{\rho}_f + \widehat{\varphi}_1 \widehat{\rho}_{s1} / \widehat{\rho}_f \right\} + \widehat{\varphi}_2 \widehat{\rho}_{s2} / \widehat{\rho}_f \right] + \widehat{\varphi}_3 \widehat{\rho}_{s3} / \widehat{\rho}_f \right) \right)}{(1 - \widehat{\varphi}_1)^{-2.5} (1 - \widehat{\varphi}_2)^{-2.5} (1 - \widehat{\varphi}_3)^{-2.5}} \right) \\
 * &\left((1 - \widehat{\varphi}_3) \left[(1 - \widehat{\varphi}_1) \left\{ (1 - \widehat{\varphi}_2) \widehat{\rho}_f + \widehat{\varphi}_1 c_{ps1} \widehat{\rho}_{s1} / \widehat{\rho}_f \right\} + \widehat{\varphi}_2 c_{ps2} \widehat{\rho}_{s2} / \widehat{\rho}_f \right] + \widehat{\varphi}_3 c_{ps3} \widehat{\rho}_{s3} / \widehat{\rho}_f \right) \\
 * &\frac{Mn}{\left((1 - \widehat{\varphi}_3) \left[(1 - \widehat{\varphi}_1) \left\{ (1 - \widehat{\varphi}_2) \widehat{\rho}_f + \widehat{\varphi}_1 \widehat{\rho}_{s1} / \widehat{\rho}_f \right\} + \widehat{\varphi}_2 \widehat{\rho}_{s2} / \widehat{\rho}_f \right] + \widehat{\varphi}_3 \widehat{\rho}_{s3} / \widehat{\rho}_f \right)} \\
 \text{Re} * &\left(\frac{(1 - \widehat{\varphi}_1)^{-2.5} (1 - \widehat{\varphi}_2)^{-2.5} (1 - \widehat{\varphi}_3)^{-2.5}}{\left((1 - \widehat{\varphi}_2) \left(1 - \widehat{\varphi}_1 + \widehat{\varphi}_1 \left(\widehat{\rho}_{s1} / \widehat{\rho}_f \right) + \widehat{\varphi}_2 \left(\widehat{\rho}_{s2} / \widehat{\rho}_f \right) \right) \right)} H_{ij} (\widetilde{\psi}_{ij} - \varepsilon) \left\{ \widehat{u}^{(n+1/2)}_{ij} \frac{H_{ij+1} - H_{ij-1}}{2k} + \widehat{v}^{(n+1/2)}_{ij} \frac{H_{i+1j} - H_{i-1j}}{2h} \right\} \right. \\
 - \widehat{u}^{(n+1/2)}_{ij} &\left(\frac{\widehat{\theta}^{(n+1/2)}_{i+1j} - \widehat{\theta}^{(n+1/2)}_{i-1j}}{2h} \right) - \widehat{v}^{(n+1/2)}_{ij} \left(\frac{\widehat{\theta}^{(n)}_{ij+1} - \widehat{\theta}^{(n)}_{ij-1}}{2k} \right) - \\
 \text{Pr} * &\left(\frac{\left(\left((1 - \widehat{\varphi}_3) \left[(1 - \widehat{\varphi}_1) \left\{ (1 - \widehat{\varphi}_2) \widehat{\rho}_f + \widehat{\varphi}_1 \widehat{\rho}_{s1} / \widehat{\rho}_f \right\} + \widehat{\varphi}_2 \widehat{\rho}_{s2} / \widehat{\rho}_f \right] + \widehat{\varphi}_3 \widehat{\rho}_{s3} / \widehat{\rho}_f \right) \right)}{(1 - \widehat{\varphi}_1)^{-2.5} (1 - \widehat{\varphi}_2)^{-2.5}} \right) \\
 * &\left((1 - \widehat{\varphi}_3) \left[(1 - \widehat{\varphi}_1) \left\{ (1 - \widehat{\varphi}_2) \widehat{\rho}_f + \widehat{\varphi}_1 c_{ps1} \widehat{\rho}_{s1} / \widehat{\rho}_f \right\} + \widehat{\varphi}_2 c_{ps2} \widehat{\rho}_{s2} / \widehat{\rho}_f \right] + \widehat{\varphi}_3 c_{ps3} \widehat{\rho}_{s3} / \widehat{\rho}_f \right) \\
 \text{Ec} &\left\{ \left(\frac{\widehat{u}^{(n+1/2)}_{ij+1} - \widehat{u}^{(n+1/2)}_{ij-1}}{2k} + \frac{\widehat{v}^{(n+1/2)}_{i+1j} - \widehat{v}^{(n+1/2)}_{i-1j}}{2h} \right)^2 + 4 \left(\frac{\widehat{u}^{(n+1/2)}_{i+1j} - \widehat{u}^{(n+1/2)}_{i-1j}}{2h} \right)^2 \right\}
 \end{aligned} \tag{13}$$

$$\frac{\widetilde{\psi}^{(n+1)}_{i-1j} + \widetilde{\psi}^{(n+1)}_{i+1j} - 2\widetilde{\psi}^{(n+1)}_{ij}}{h^2} + \frac{\widetilde{\psi}^{(n+1)}_{ij-1} + \widetilde{\psi}^{(n+1)}_{ij+1} - 2\widetilde{\psi}^{(n+1)}_{ij}}{k^2} = -\widehat{w}^{(n+1/2)}_{ij}, \tag{14}$$

$$\widehat{u}^{(n+1)}_{ij} = \frac{-\widetilde{\psi}^{(n+1)}_{ij-1} + \widetilde{\psi}^{(n+1)}_{ij+1}}{2k}, \tag{15}$$

$$\widehat{v}^{(n+1)}_{ij} = -\frac{\widetilde{\psi}^{(n+1)}_{i+1j} - \widetilde{\psi}^{(n+1)}_{i-1j}}{2h}, \tag{16}$$

$$\frac{\widehat{w}_{ij}^{(n+1)} - \widehat{w}_{ij}^{(n+1/2)}}{\delta t/2} = \text{Re} * \left(\frac{(1 - \widehat{\varphi}_1)^{-2.5} (1 - \widehat{\varphi}_2)^{-2.5} (1 - \widehat{\varphi}_3)^{-2.5}}{\left((1 - \widehat{\varphi}_3) \left[(1 - \widehat{\varphi}_1) \left\{ (1 - \widehat{\varphi}_2) \widehat{\rho}_f + \widehat{\varphi}_1 \widehat{\rho}_{s1} / \widehat{\rho}_f \right\} + \widehat{\varphi}_2 \widehat{\rho}_{s2} / \widehat{\rho}_f \right] + \widehat{\varphi}_3 \widehat{\rho}_{s3} / \widehat{\rho}_f \right)} \right) \left\{ \frac{\widehat{w}_{i-1j}^{(n+1/2)} - 2\widehat{w}_{ij}^{(n+1/2)} + \widehat{w}_{i+1j}^{(n+1/2)}}{h^2} + \frac{\widehat{w}_{ij-1}^{(n+1)} - 2\widehat{w}_{ij}^{(n+1)} + \widehat{w}_{ij+1}^{(n+1)}}{k^2} \right\} + \frac{Mn}{\left((1 - \widehat{\varphi}_3) \left[(1 - \widehat{\varphi}_1) \left\{ (1 - \widehat{\varphi}_2) \widehat{\rho}_f + \widehat{\varphi}_1 \widehat{\rho}_{s1} / \widehat{\rho}_f \right\} + \widehat{\varphi}_2 \widehat{\rho}_{s2} / \widehat{\rho}_f \right] + \widehat{\varphi}_3 \widehat{\rho}_{s3} / \widehat{\rho}_f \right)} \tag{17}$$

$$+ H_{i,j} \left\{ \frac{H_{i,j+1} - H_{i,j-1}}{2k} \frac{\widehat{\theta}_{i+1j}^{(n+1)} - \widehat{\theta}_{i-1j}^{(n+1)}}{2h} - \frac{H_{i+1j} - H_{i-1j}}{2h} \frac{\widehat{\theta}_{ij+1}^{(n+1)} - \widehat{\theta}_{ij-1}^{(n+1)}}{2k} \right\} - \widehat{u}_{ij}^{(n+1/2)} \left(\frac{\widehat{w}_{i+1j}^{(n+1)} - \widehat{w}_{i-1j}^{(n+1)}}{2h} \right) - \widehat{v}_{ij}^{(n+1/2)} \left(\frac{\widehat{w}_{ij+1}^{(n+1)} - \widehat{w}_{ij-1}^{(n+1)}}{2k} \right) \\ \frac{\widehat{\theta}_{ij}^{(n+1)} - \widehat{\theta}_{ij}^{(n+1/2)}}{\delta t/2} = \left\{ \frac{\widehat{\theta}_{i-1j}^{(n+1/2)} - 2\widehat{\theta}_{ij}^{(n+1/2)} + \widehat{\theta}_{i+1j}^{(n+1/2)}}{h^2} + \frac{\widehat{\theta}_{ij-1}^{(n+1)} + \widehat{\theta}_{ij+1}^{(n+1)} - 2\widehat{\theta}_{ij}^{(n+1)}}{k^2} \right\} + \text{Pr} * \left(\frac{\left((1 - \widehat{\varphi}_3) \left[(1 - \widehat{\varphi}_1) \left\{ (1 - \widehat{\varphi}_2) \widehat{\rho}_f + \widehat{\varphi}_1 \widehat{\rho}_{s1} / \widehat{\rho}_f \right\} + \widehat{\varphi}_2 \widehat{\rho}_{s2} / \widehat{\rho}_f \right] + \widehat{\varphi}_3 \widehat{\rho}_{s3} / \widehat{\rho}_f \right)}{(1 - \widehat{\varphi}_1)^{-2.5} (1 - \widehat{\varphi}_2)^{-2.5} (1 - \widehat{\varphi}_3)^{-2.5}} \right) * \left((1 - \widehat{\varphi}_3) \left[(1 - \widehat{\varphi}_1) \left\{ (1 - \widehat{\varphi}_2) \widehat{\rho}_f + \widehat{\varphi}_1 c_{ps1} \widehat{\rho}_{s1} / \widehat{\rho}_f \right\} + \widehat{\varphi}_2 c_{ps2} \widehat{\rho}_{s2} / \widehat{\rho}_f \right] + \widehat{\varphi}_3 c_{ps3} \widehat{\rho}_{s3} / \widehat{\rho}_f \right) \\ * \frac{Mn}{\left((1 - \widehat{\varphi}_3) \left[(1 - \widehat{\varphi}_1) \left\{ (1 - \widehat{\varphi}_2) \widehat{\rho}_f + \widehat{\varphi}_1 \widehat{\rho}_{s1} / \widehat{\rho}_f \right\} + \widehat{\varphi}_2 \widehat{\rho}_{s2} / \widehat{\rho}_f \right] + \widehat{\varphi}_3 \widehat{\rho}_{s3} / \widehat{\rho}_f \right)} \text{Re} * \left(\frac{(1 - \widehat{\varphi}_1)^{-2.5} (1 - \widehat{\varphi}_2)^{-2.5} (1 - \widehat{\varphi}_3)^{-2.5}}{\left((1 - \widehat{\varphi}_3) \left[(1 - \widehat{\varphi}_1) \left\{ (1 - \widehat{\varphi}_2) \widehat{\rho}_f + \widehat{\varphi}_1 \widehat{\rho}_{s1} / \widehat{\rho}_f \right\} + \widehat{\varphi}_2 \widehat{\rho}_{s2} / \widehat{\rho}_f \right] + \widehat{\varphi}_3 \widehat{\rho}_{s3} / \widehat{\rho}_f \right)} \right) H_{i,j} (\widehat{\psi}_{i,j} - \epsilon) \\ \left\{ \widehat{u}_{ij}^{(n+1/2)} \frac{H_{i,j+1} - H_{i,j-1}}{2k} + \widehat{v}_{ij}^{(n+1/2)} \frac{H_{i+1j} - H_{i-1j}}{2h} \right\} - \widehat{u}_{ij}^{(n+1/2)} \left(\frac{\widehat{\theta}_{i+1j}^{(n+1/2)} - \widehat{\theta}_{i-1j}^{(n+1/2)}}{2h} \right) - \widehat{v}_{ij}^{(n+1/2)} \left(\frac{\widehat{\theta}_{ij+1}^{(n+1)} - \widehat{\theta}_{ij-1}^{(n+1)}}{2k} \right) - \text{Pr} * \left(\frac{(1 - \widehat{\varphi}_2) (1 - \widehat{\varphi}_1 + \widehat{\varphi}_1 \left(\widehat{\rho}_{s1} / \widehat{\rho}_f \right) + \widehat{\varphi}_2 \left(\widehat{\rho}_{s2} / \widehat{\rho}_f \right))}{(1 - \widehat{\varphi}_1)^{-2.5} (1 - \widehat{\varphi}_2)^{-2.5}} \right) * \left((1 - \widehat{\varphi}_3) \left[(1 - \widehat{\varphi}_1) \left\{ (1 - \widehat{\varphi}_2) \widehat{\rho}_f + \widehat{\varphi}_1 c_{ps1} \widehat{\rho}_{s1} / \widehat{\rho}_f \right\} + \widehat{\varphi}_2 c_{ps2} \widehat{\rho}_{s2} / \widehat{\rho}_f \right] + \widehat{\varphi}_3 c_{ps3} \widehat{\rho}_{s3} / \widehat{\rho}_f \right) \\ Ec \left\{ \left(\frac{\widehat{u}_{ij+1}^{(n+1/2)} - \widehat{u}_{ij-1}^{(n+1/2)}}{2k} + \frac{\widehat{v}_{i+1j}^{(n+1/2)} - \widehat{v}_{i-1j}^{(n+1/2)}}{2h} \right)^2 + 4 \left(\frac{\widehat{u}_{i+1j}^{(n+1/2)} - \widehat{u}_{i-1j}^{(n+1/2)}}{2h} \right)^2 \right\} \tag{18}$$

The iteration scheme is terminated when the criterion:

$$\max \left\{ \text{abs} \left(\tilde{\psi}_{ij}^{(n+1)} - \tilde{\psi}_{ij}^{(n)} \right), \text{abs} \left(w_{ij}^{(n+1)} - w_{ij}^{(n)} \right), \text{abs} \left(\theta_{ij}^{(n+1)} - \theta_{ij}^{(n)} \right) \right\} < TOL$$

is reached, indicating that a steady-state solution has been achieved. For the purpose of this study, the present problem assumes $TOL < 10^{-6}$.

4.1. Flow chart of our numerical approach

The computational model for the concerned technique is represented in Fig. 2.

4.2. Testing the effectiveness of the numerical scheme

To ensure that our numerical technique is trustworthy and accurate, we compare our numerical results for horizontal velocity profiles to those obtained by Asia et al. [49]. The horizontal velocity profiles are the fluctuations of the horizontal component of the fluid velocity on a vertical axis. We examine the limiting case when $\hat{\varphi}_1 = \hat{\varphi}_2 = 0$, $Mn = 0$, indicating that there is no heat generation, no magnetic field, and no buoyancy force. In this case, the fluid flow is driven solely by the movement of one of the lids of the cavity. We analyze the horizontal velocity profiles along three distinct horizontal lines which are located at $y = 0.25, 0.50,$ and 0.75 , whereas

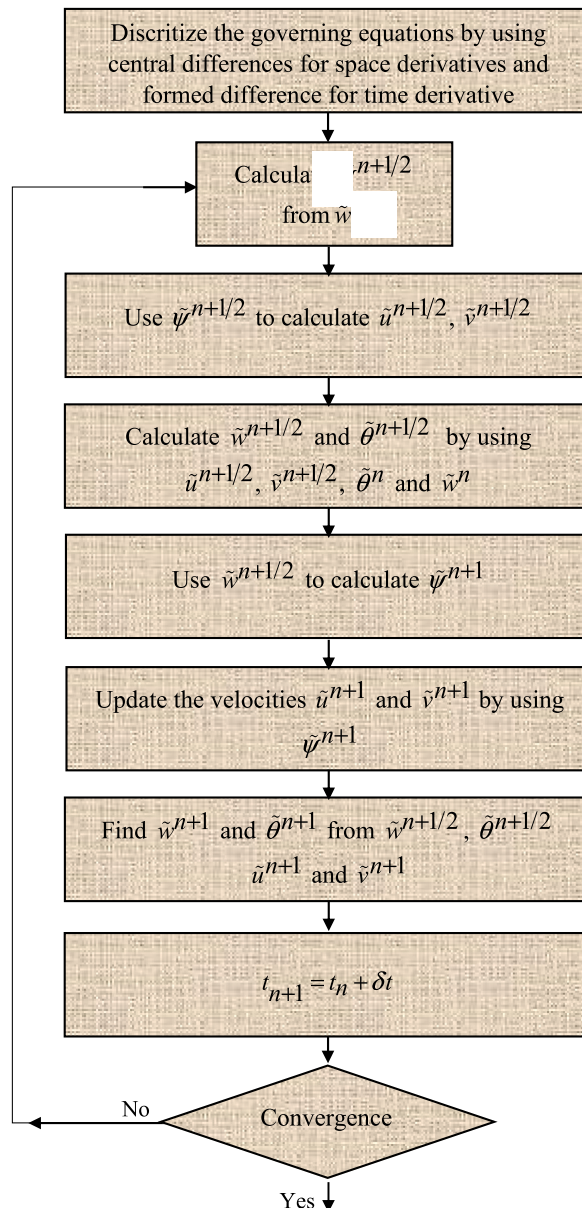


Fig. 2. A flow Chart of the Pseudo-Transient Approach.

y is the vertical coordinates normalized by the height of the lid-driven cavity (see Fig. 3).

To validate our code further, we implement it to the renowned problem of natural convection inside a cavity, which was explored by Chen et al. [51] and D. Davis [52] using the Lattice Boltzmann method and the finite difference method respectively. Table 2 indicates that the values of the Nusselt number that we find through our numerical investigation correspond to those derived from earlier studies extremely well.

The base fluid in this work is water, and the nanostructures are a mixture of Ag, Al₂O₃, and TiO₂. The nanoparticles are incorporated into the base fluid to improve thermal conductivity and heat transfer. In our simulations, we take $\varepsilon = 0.02$ to symbolize the thermophysical characteristics of the nanofluid. The water attributes used throughout our simulations are based on $Pr = 6.2$. The Reynolds number is a dimensionless parameter that quantifies the ratio of inertial to viscous forces in a fluid flow. The Eckert number is another dimensionless quantity that reflects the ratio of kinetic energy to enthalpy change in a fluid flow. A very small Reynolds number results in an exceptionally low Eckert number (e.g., 10^{-5}), indicating that viscous forces dominate and kinetic energy is negligible. Table 3 depicts the fundamental properties of the nanomaterials and base fluid utilized in this work, such as density, particle size, specific heat, thermal conductivity, and viscosity.

On the other hand, Fig. 4 demonstrates, how our numerical results converge with regard to the step size, which is the distance between two consecutive grid points. The numerical findings converge when the step size is decreased. This shows that our numerical technique is stable and does not generate spurious oscillations or divergences. Furthermore, it also indicates that the numerical findings are not affected by the grid size, which is the total number of grid points utilized to discretize the domain. This means that when the grid size is extended beyond a certain point, the numerical results do not change significantly.

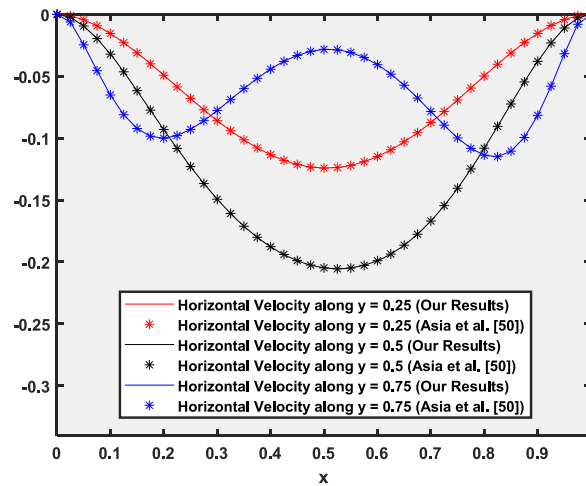


Fig. 3. Comparison of numerical results with Shih and Tan [50] for the fixed $Re = 10, Mn = 0, Pr = 6.2, Ec = 0, \hat{\varphi}_1 = 0.0, \hat{\varphi}_2 = 0.02, \hat{\varphi}_2 = 0.02$.

Table 2
Our results versus literature: A quality analysis.

Re	Average Nu for the Hot Wall		
	Lattice Boltzmann's approach [51]	Finite Difference approach (D. Davis [52])	Our Approach
10^3	1.1192	1.1181	1.1182
10^4	2.2531	2.2432	2.2481

Table 3
Thermal and physical features of water and nanomaterials (Ag-Al₂O₃-TiO₂).

	$C_p (Jkg^{-1}K^{-1})$	$\sigma (S \times m^{-1})$	$\hat{\rho} (kgm^{-3})$	$\beta (K^{-1})$	$k (Wm^{-1}K^{-1})$
Water	4179	0.05	997.1	21×10^{-5}	0.613
Silver(Ag)	235	3.6×10^7	8933	1.89×10^{-5}	429
Aluminum Oxide (Al ₂ O ₃)	765	1×10^{-1}	3970	0.85×10^{-5}	40
Titanium Dioxide (TiO ₂)	686	1×10^{-12}	5200	0.90×10^{-5}	8.95

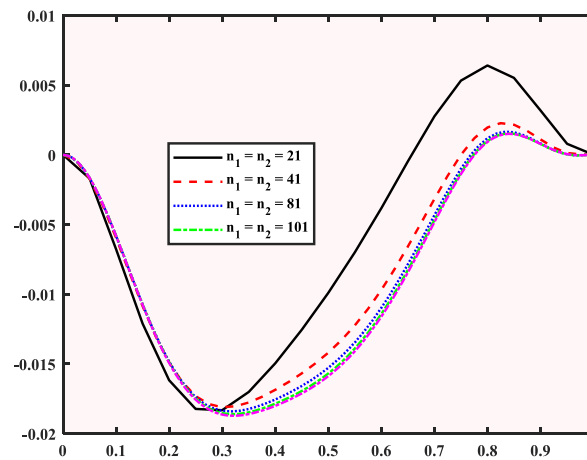


Fig. 4. Grid Independence Analysis for the Normal Velocity Distribution along the Line $y = 0.5$.

5. Results and discussion

The results displayed in the various figures and tables are presented and discussed in the next section. The figures exhibit streamlines and isotherms, which are visual depictions of the fluid flow and temperature distribution in the lid-driven cavity. The tables display the Nu and CfRe values along the upper and bottom horizontal walls. The CfRe measures the shear stress exerted by the fluid on the wall, whereas the Nu indicates the rate of heat transfer across the wall. The findings are for the scenario when both horizontal lids of the square enclosure slide in opposite directions, yielding shear-driven flow in the cavity, with the lower lid moving along the bottom wall of the cavity in the +ve x-axis. Also investigate how various basic factors, like the nanoparticle volume fraction ($0 \leq \hat{\varphi}_1, \hat{\varphi}_2, \hat{\varphi}_3 \leq 0.20$), which is the ratio of the volume of nanostructures to the total volume of nanofluid; the confined magnetic field in the form of strips ($0.2 \leq \xi \leq 0.3, 0.7 \leq \xi \leq 0.8$, and $0 \leq \eta \leq 1$) and ($0.2 \leq \eta \leq 0.3, 0.7 \leq \eta \leq 0.8$, and $0 \leq \xi \leq 1$), which somewhat is a region of the uniform magnetic field employed to a part of the cavity; the Reynolds number (dimensionless parameter that identifies the fluid flow regime); and the magnetic number (another dimensionless parameter that characterizes the strength of the magnetic field in the flow regime). These parameters are all dimensionless groups of material and flow properties, and/or geometric dimensions of the domain. The traditional way of studying the flow and thermal characteristics of fluid dynamics problems is to specify the values of these dimensionless groups rather than specifying the particular fluid properties and the dimensions of the domain. Obviously, the results obtained in this way are applicable to the flow problems with particular values of material properties and the dimensions of the domain, falling in the ranges considered in the studies. In the present work, we have computed our results for the following values of the governing parameters ($1 \leq Re \leq 35$), and ($0 \leq Mn \leq 700$). The flow field is further influenced by the localized magnetic field in four stripes; two horizontal and two verticals with a uniform width (1 unit), which split the cavity into nine sub-regions. It also explores how the Nu and the CfRe are influenced by the tri-hybrid (Ag, Al_2O_3 , and TiO_2) nature of the fluid. Pressure drop calculations are considered in the ducts (for example, exhaust air vents) where the pressure is higher on one side of the vent than it is on the other. For the present problem, there is no imposed pressure gradient on the flow. Therefore, such calculations do not apply to the problem under consideration.

Our study aims to explore how two forces influence the fluid dynamics and thermal behavior of the problem. These forces are: (i) the inertial force caused by the lid moving on top of the enclosure, and (ii) the Lorentz force generated by a magnet outside the enclosure. Moreover, the low-density fluid that flows upward from heated walls due to the thermal buoyancy force is opposed by the high-density fluid that results from the strong magnetic force. We will examine how these forces interact and affect the fluid motion and heat transfer in the problem.

5.1. The implications of the magnetic source

The significance of magnetic field intensity, as described by the horizontal and vertical strips in the regions ($0.2 < \xi < 0.3, 0.7 < \xi < 0.8, 0 < \eta < 1$ and $0.2 < \eta < 0.3, 0.7 < \eta < 0.8, 0 < \xi < 1$) on the fluids flow can be illustrated in Fig. 5 This study examines the effect of magnetic fields on the flow and temperature fields in a lid-driven cavity. The magnetic fields are applied in the form of vertical and horizontal strips inside the cavity. The rotation of vortices depends on the movement of the top and bottom lids of the enclosure that are driven by some external mechanical setup. In the case of no magnetic force, two vortices are almost symmetric about the line in the flow field. When the magnetic fields are introduced, they generate body forces that interact with the externally applied force and cause different effects on the flow and temperature fields. The intensity of the magnetic sources first elongates the existing vortex which eventually breaks down to create two new smaller and weaker vortices (in the lower and upper half of the cavity) rotating in clockwise or counter-clockwise directions. As the intensity increases, more vortices are formed in different parts of the cavity, spinning in different directions depending on the orientation of the net force acting on the fluid in that particular region.

Fig. 6 illustrates the effect of the parameter (Mn) on the temperature distribution in the flow field. Without any magnetic force, most of the isotherms have a smooth and red-colored pattern, indicating a high temperature. The isotherms are also denser near the top and bottom walls of the cavity, due to the natural convection caused by the heated top lid and the cooled bottom lid. With the magnetic

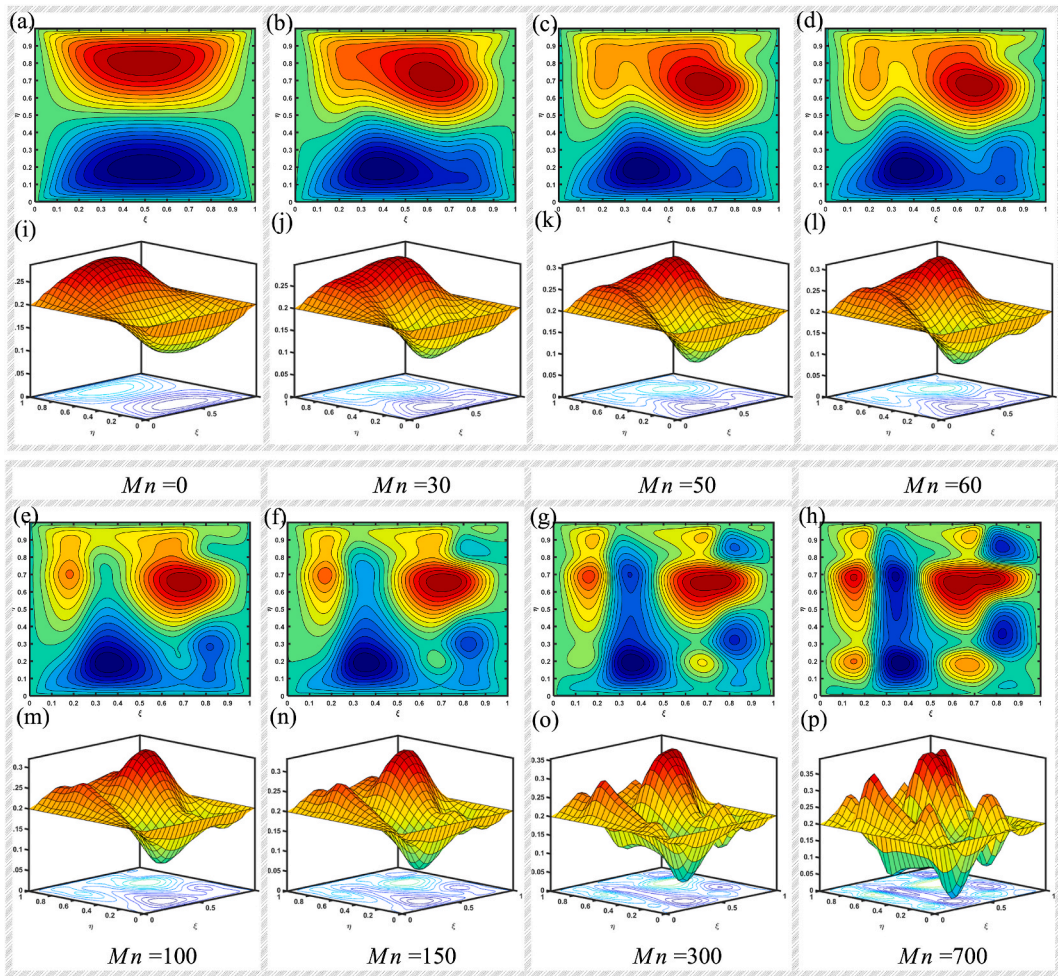


Fig. 5. Flow representation by streamlines (a-h) and stream surfaces (i-p) for $Re = 5$, $Pr = 6.2$, $L = 0.00$, $Ec = 10^{-5}$, $\widehat{\varphi}_1 = 0.05$, $\widehat{\varphi}_2 = 0.02$, $\widehat{\varphi}_2 = 0.02$ and different Mn .

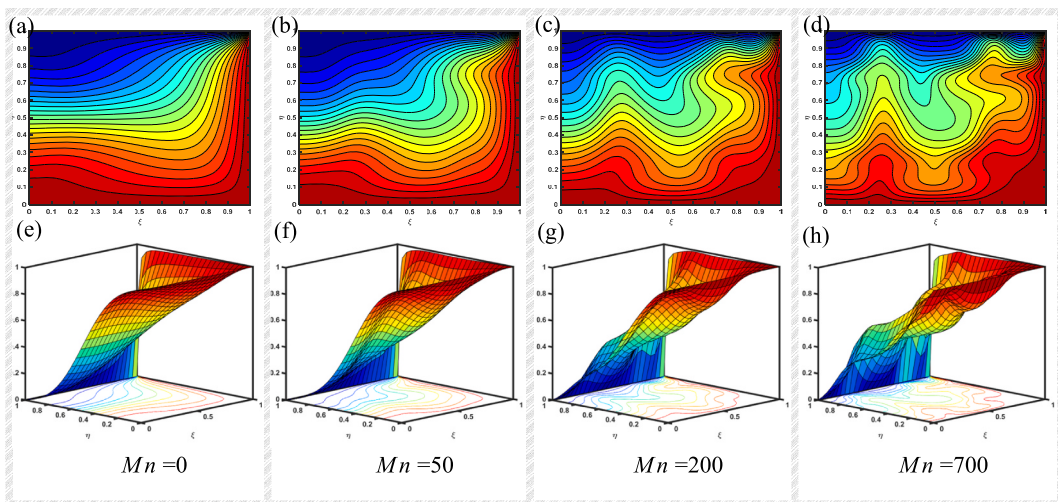


Fig. 6. Isotherms (a-d) and temperature fields (e-h) for the flow with different $Re = 5$, $Pr = 6.2$, $L = 0.00$, $Ec = 10^{-5}$, $\widehat{\varphi}_1 = 0.05$, $\widehat{\varphi}_2 = 0.02$, $\widehat{\varphi}_2 = 0.02$, and Mn .

force, however, the temperature distribution becomes more irregular and uneven. This is because the new vortices generated in the flow enhance the mixing of fluid bodies with different temperatures, which disturbs the thermal signature across the enclosure.

5.2. Impact of the Reynolds number

Fig. 7 shows how the flow pattern changes with the Reynolds number, which is a dimensionless parameter that measures the ratio of inertial forces to viscous forces in the fluid. For a given cavity size and fluid properties, a higher Reynolds number implies a higher velocity of the lids. Therefore, the Reynolds number can be used to characterize the lid speed. When the Reynolds number is low ($Re = 1$), the flow field consists of two symmetrical primary vortices that rotate in opposite directions along the top and bottom horizontal walls of the cavity. These vortices are driven by the shear stress induced by the moving lids. As the Reynolds number increases, the primary vortices become distorted and deformed due to the increased inertial forces. It is important to note that one of the terms in the governing equations is a product of the magnetic parameters and the Reynolds number. This means that a higher Reynolds number will also increase the effect of this term on the flow dynamics. Consequently, the Reynolds number and the magnetic parameter will have a similar influence on the flow pattern in some aspects.

Fig. 8 depicts how the temperature distribution changes with the Re . As explained before, the lids move faster when Re increased, assuming that the fluid properties and the cavity size are constant. The higher lid velocity will induce stronger shear stress on the fluid layer near the walls, which will cause a stronger blending of fluid bodies with different temps. This will disrupt any smooth or uniform pattern of the isotherms and create more irregular and uneven temperature contours.

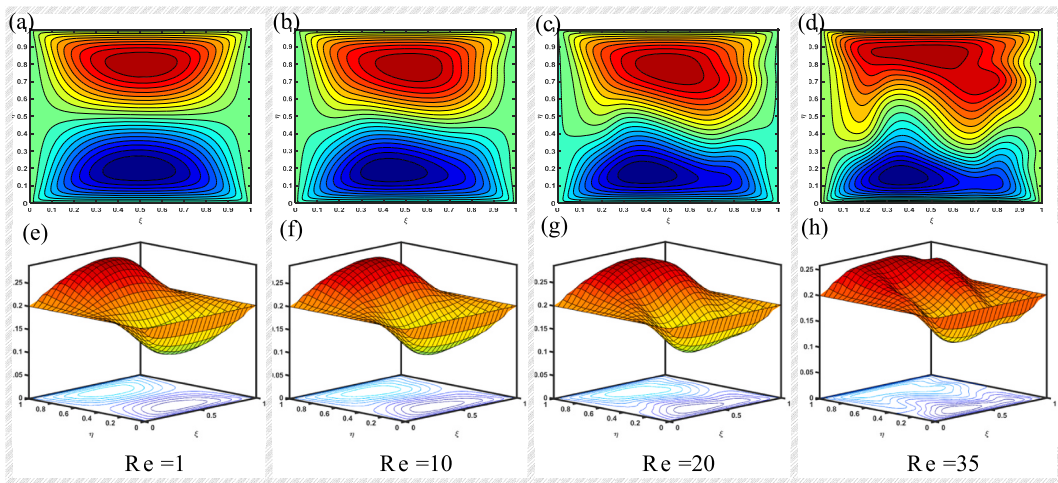


Fig. 7. Flow representation by streamlines (a-d) and stream surfaces (e-h) for $Mn = 5, Pr = 6.2, L = 0.00, Ec = 10^{-5}, \hat{\varphi}_1 = 0.05, \hat{\varphi}_2 = 0.02, \hat{\varphi}_2 = 0.02$ and different Re .

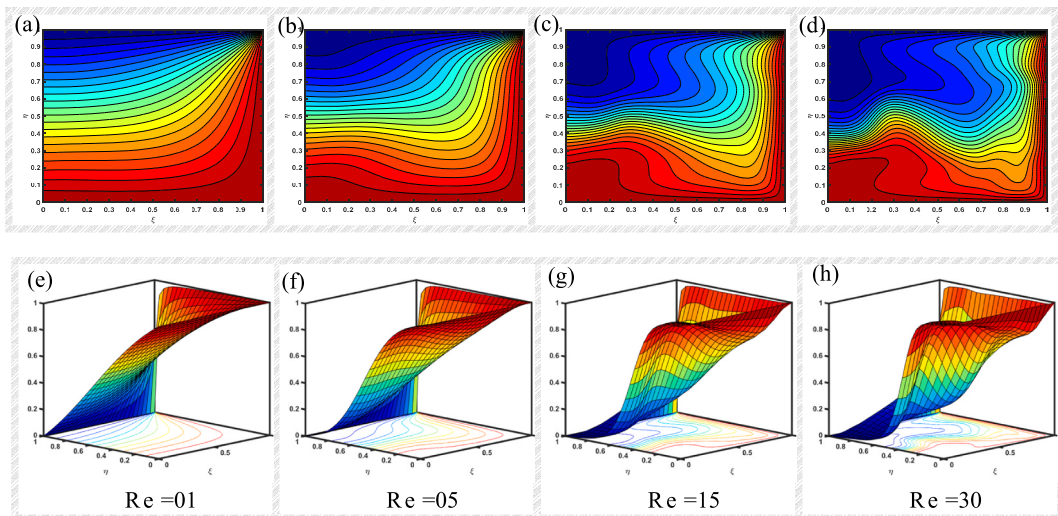


Fig. 8. Isotherms (a-d) and temperature fields (e-h) for the flow with $Mn = 5, Pr = 6.2, L = 0.00, Ec = 10^{-5}, \hat{\varphi}_1 = 0.05, \hat{\varphi}_2 = 0.02, \hat{\varphi}_2 = 0.02$ and different Re .

5.3. Impact of localization

An obvious point to ponder may be the role of the width of the magnetic field in the present problem. To understand this, we consider the strips defined by: $(0.2 - L < \xi < 0.3 + L, 0.7 - L < \xi < 0.8 + L, 0 < \eta < 1)$ and $(0.2 - L < \eta < 0.3 + L, 0.7 - L < \eta < 0.8 + L, 0 < \xi < 1)$, within the flow field. It is obvious to note that the parameter L determines the width of the strips, obviously, $L = 0.2$, corresponds to the case when the magnetic field is occupying the whole cavity whereas $L = 0.0$ when the magnetic field is confined to the strips $(0.2 < \xi < 0.3, 0.7 < \xi < 0.8, 0 < \eta < 1)$ and $(0.2 < \eta < 0.3, 0.7 < \eta < 0.8, 0 < \xi < 1)$. It is not seen much impact on the flow and temperature distributions when the magnetic field occupies the whole flow field. However, Fig. 9 depicts that the confinement of the magnetic field intensity gives rise to new vortices while eliminating the primary vortices. The isotherms, on the other hand, undergo a zig-zag behavior which is obviously due to the rigorous mix of the fluid layers at different temperatures (see Fig. 10).

5.4. Nusselt number and skin-friction dependence on different parameters

In this subsection, we study the effects of the governing parameters magnetic number (Mn) and Reynolds number (Re) on the skin friction factor ($CfRe$) and Nusselt number (Nu). We plot the Nu and $CfRe$ profiles in Figs. 11 and 12, respectively. It can be observed that the magnetic parameter (Mn) has a significant impact on Nu in the middle of the cavity. However, the localization of the magnetic field (L) has a negligible impact on the $CfRe$ in the flow field. On the other hand, the Reynolds number (Re) leads to a substantial decrease in the Nusselt number (Nu) and it reaches its minimum value near the right bottom corner of the cavity for higher values of the Re . Regarding

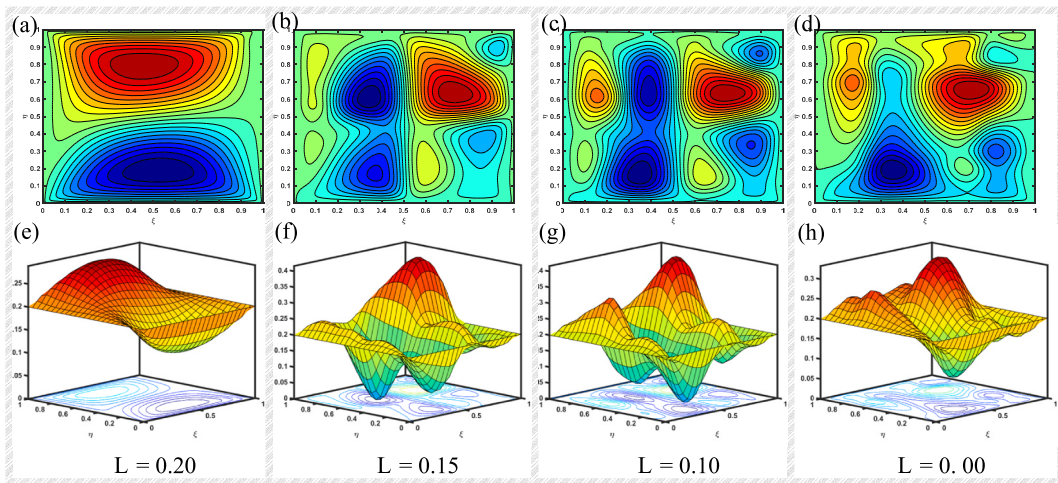


Fig. 9. Streamlines (a-d) and stream surfaces (e-h) with different values of the magnetic strip length (L) for $Mn = 150, Re = 5, Pr = 6.2, Ec = 10^{-5}, \hat{\varphi}_1 = 0.05, \hat{\varphi}_2 = 0.02, \hat{\varphi}_2 = 0.02$.

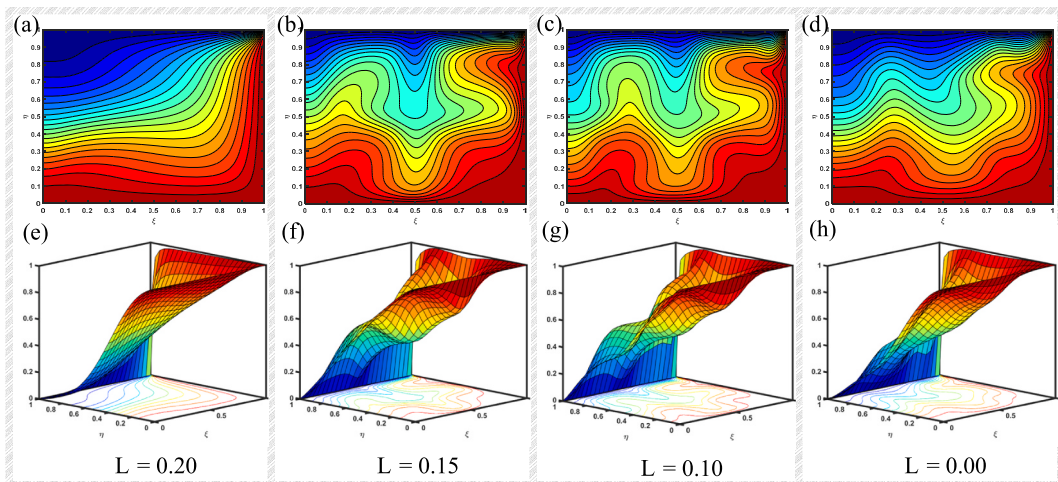


Fig. 10. Isotherms (a-d) and temperature fields (e-h) with different values of the magnetic strip length (L) for $Mn = 150, Re = 5, Pr = 6.2, Ec = 10^{-5}, \hat{\varphi}_1 = 0.05, \hat{\varphi}_2 = 0.02, \hat{\varphi}_2 = 0.02$.

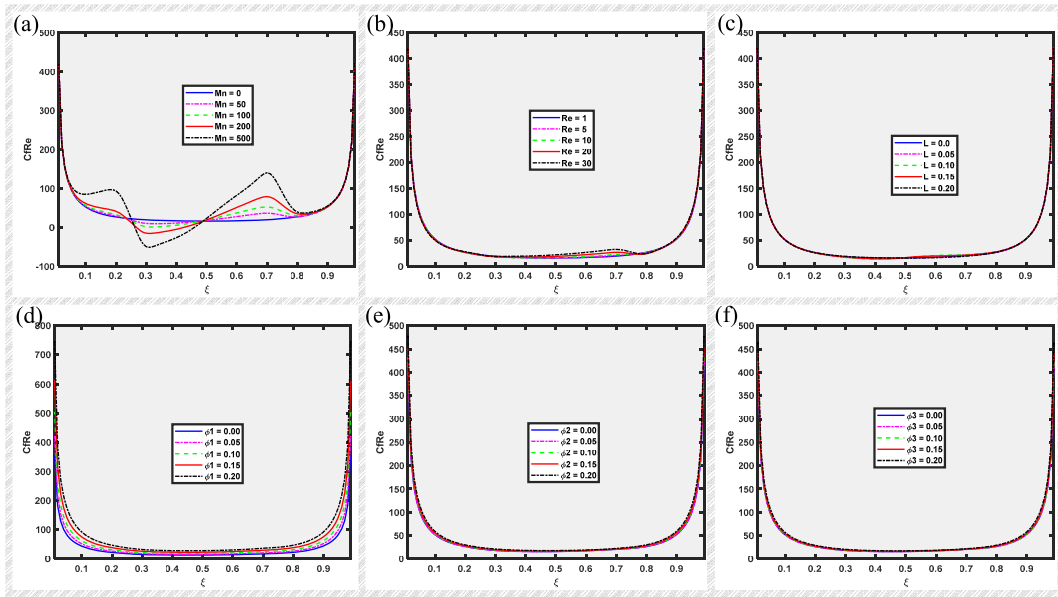


Fig. 11. Dependence of CfRe (a–f) on Various Factors for fixed $Mn = 5$, $Re = 5$, $L = 0$, $Pr = 6.2$, $Ec = 10^{-5}$, $\hat{\varphi}_1 = 0.05$, $\hat{\varphi}_2 = 0.02$, $\hat{\varphi}_3 = 0.02$.

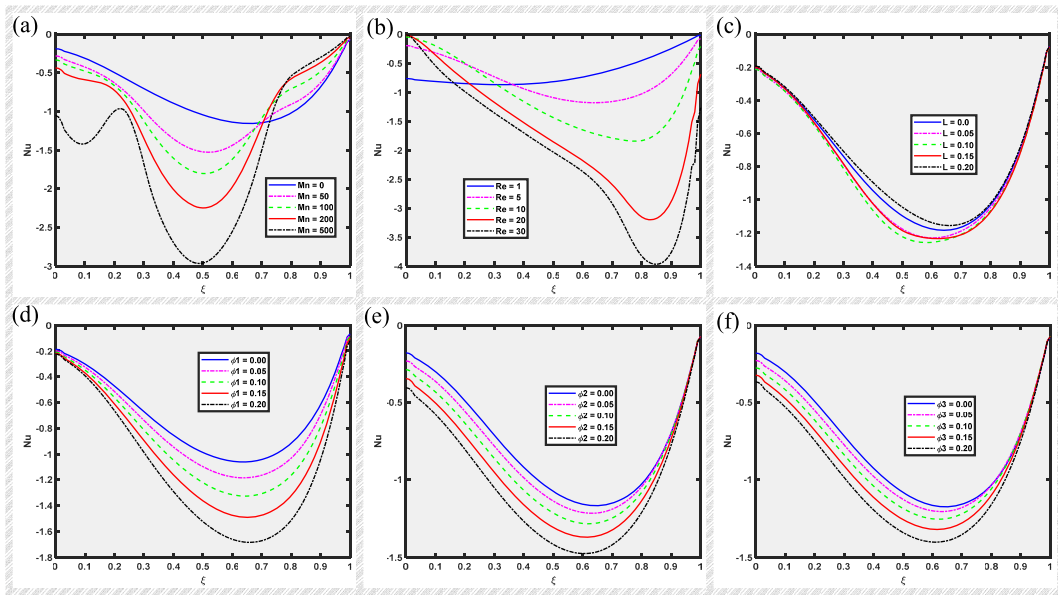


Fig. 12. Dependence of Nu (a–f) on Various Factors for fixed $Mn = 5$, $Re = 5$, $L = 0$, $Pr = 6.2$, $Ec = 10^{-5}$, $\hat{\varphi}_1 = 0.05$, $\hat{\varphi}_2 = 0.02$, $\hat{\varphi}_3 = 0.02$.

the CfRe, we discover that both factors affect CfRe in a similar qualitative manner. The quantitative effect might vary slightly depending on the parameter values. Moreover, the nano nature of the fluid has a very marginal impact on skin friction (CfRe). As expected, φ_1 , φ_2 and φ_3 has a notable impact on the Nu with a relatively minor effect on the CfRe. However, compared to φ_2 and φ_3 the Nusselt number is more sensitive to φ_1 by inherent thermophysical characteristics of the nanomaterials. We also notice that the localization or confinement of the magnetic field does not always increase or decrease the Nusselt number (Nu) uniformly. Therefore, we conclude that there exists an optimal width of the magnetic corridor that maximizes the Nu, which could be a topic for future research.

5.5. Effect of different parameters on physical quantities

In this section, we examine the effects of skin friction (CfRe) and Nusselt number (Nu) with different parameters. Table 4 reveals that both the Nu and the CfRe increase when the magnetic field strength is higher. The Nu increases more dramatically, almost doubling its initial values, while the CfRe only rises by 46%. In contrast, Table 5 reveals that changing the Re has a notable effect on Nu

Table 4Influence of magnetic numbers on Nu and CfRe for $Re = 10$; $Mn = 20$, $L = 0$, $Pr = 6.2$, $Ec = 10^{-5}$, $\hat{\varphi}_1 = 0.05$, $\hat{\varphi}_2 = 0.02$, $\hat{\varphi}_2 = 0.02$.

Mn	Nu	CfRe
0	0.7641	46.7321
100	0.9829	50.6678
200	1.1326	53.9448
300	1.2755	57.4249
500	1.5268	66.0112

Table 5Influence of Reynolds numbers on Nu and CfRe for $Re = 10$; $Mn = 20$, $L = 0$, $Pr = 6.2$, $Ec = 10^{-5}$, $\hat{\varphi}_1 = 0.05$, $\hat{\varphi}_2 = 0.02$, $\hat{\varphi}_2 = 0.02$.

Re	Nu	CfRe
1	0.6724	46.7360
5	0.7883	46.8343
10	1.1146	47.0443
20	1.7171	47.9937
30	2.0530	49.7855

but a minimal effect on the CfRe..

The results presented in Table 6, Table 7, and Table 8 indicate that the type of nanoparticles has a significant influence on the heat transfer rate of nanofluids. The Nu and the CfRe both increased with the addition of nanoparticles, but the magnitude of the increase varied for different types of nanoparticles. For silver(Ag), the highest increase in both the Nusselt number (55%) and the skin friction (110% almost double of Nu) was observed, implying a strong coupling between the thermal and fluid properties of the nanofluid. For Alumina Al_2O_3 and Titanium Dioxide (TiO_2), the Nusselt number increased by 33% and 25%, respectively, while the skin friction increased by 13% and 9%, respectively, suggesting a weaker coupling or a trade-off between the two properties of the nanofluid. In short, Table 4, 6–8 indicate that employing a magnetic field with a tri-hybrid nanofluid is helpful for situations involving greater efficiency of heat transfer. This observation is in line with the conclusions drawn in an excellent series of works [9–11,14].

Considering that the parameter L represents one of the geometric dimensions of the rectangular domain where the magnetic field is confined, it can be inferred (from Table 9) that the expansion of the magnetic field over a larger region of the domain results in a negligible decrease in both the Nusselt number (3%) and the skin friction factor (0.1%).

5.6. Comparison of thermal properties of the nanostructures

From Fig. 13 two main findings can be drawn: first, the average Nu (when the Lorentz force is next to the vertical wall) has a nearly linear correlation with the nanoparticle volume fraction, which means that increasing the nanoparticle concentration increases the heat transfer rate; and second, the tri-hybrid nanofluid (Ag, Al_2O_3 , and TiO_2) increases the average Nusselt number more than the conventional fluid.

5.7. The role of magnetic field intensity

Fig. 14 illustrates how the parameter A_1 and A_2 affect the average Nusselt number. It is important to note that the parameters determine the intensity of the magnetic field. Further, the Nusselt number is noted to be more dependent on A_1 and A_2 at their smaller

Table 6The Influence of Silver Nanostructure on Nu and CfRe with fixed $Re = 2$; $Mn = 5$, $L = 0$, $Pr = 6.2$, $Ec = 10^{-5}$, $\hat{\varphi}_1 = 0.05$, $\hat{\varphi}_2 = 0.02$, $\hat{\varphi}_2 = 0.02$.

$\hat{\varphi}_1$ (Silver)	Nu	CfRe
0.00	0.7093	39.4366
0.05	0.7883	46.8343
0.10	0.8781	56.1175
0.15	0.9809	67.9094
0.20	1.1002	83.0918

Table 7The Influence of Alumina Nanostructure on Nu and CfRe with fixed $Re = 2$; $Mn = 5$, $L = 0$, $Pr = 6.2$, $Ec = 10^{-5}$, $\hat{\varphi}_1 = 0.05$, $\hat{\varphi}_2 = 0.02$, $\hat{\varphi}_2 = 0.02$.

$\hat{\varphi}_2$ (Alumina)	Nu	CfRe
0.00	0.7713	46.9429
0.05	0.8177	46.9933
0.10	0.8766	48.0578
0.15	0.9479	50.0988
0.20	1.0310	53.1759

Table 8

The Influence of Titanium Dioxide Nanostructure on Nu and CfRe with fixed $Re = 2; Mn = 5, L = 0, Pr = 6.2, Ec = 10^{-5}, \hat{\varphi}_1 = 0.05, \hat{\varphi}_2 = 0.02, \hat{\varphi}_2 = 0.02$.

$\hat{\varphi}_3$ (Titanium Dioxide)	$ Nu $	$ CfRe $
0.00	0.7762	47.1886
0.05	0.8101	46.6722
0.10	0.8551	47.2824
0.15	0.9103	48.9204
0.20	0.9744	51.6055

Table 9

The Influence of Localized Magnetic Field Strips on Nu and CfRe with fixed $Re = 2; Mn = 5, L = 0, Pr = 6.2, Ec = 10^{-5}, \hat{\varphi}_1 = 0.05, \hat{\varphi}_2 = 0.02, \hat{\varphi}_2 = 0.02$.

L	$ Nu $	$ CfRe $
00	0.7883	46.8343
0.05	0.8240	47.0273
0.10	0.8444	47.1465
0.15	0.8289	47.0384
0.20	0.7644	46.7544

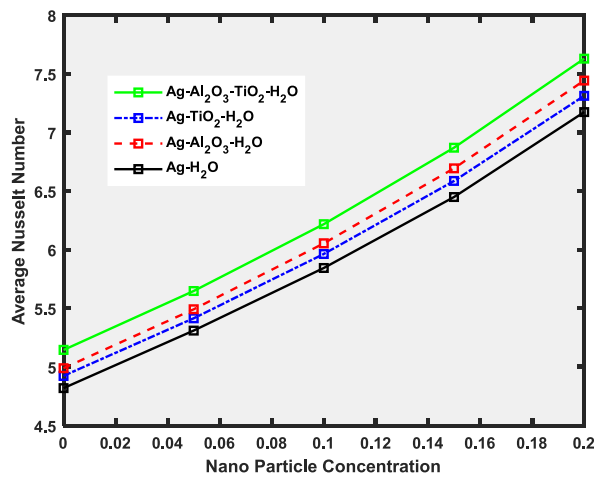


Fig. 13. Exploring the Distinctions between Double and Triple Nanofluid Mixtures with fixed $Mn = 15, Re = 15, L = 0, Pr = 6.2, Ec = 10^{-5}, \hat{\varphi}_1 = 0.05, \hat{\varphi}_2 = 0.02, \hat{\varphi}_2 = 0.02$.

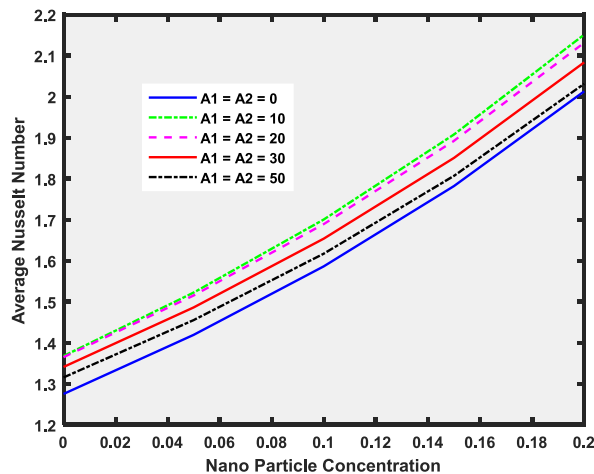


Fig. 14. Impact of the Parameter A_1 and A_2 on Average Nu with fixed $Mn = 15, Re = 15, L = 0, Pr = 6.2, Ec = 10^{-5}, \hat{\varphi}_1 = 0.05, \hat{\varphi}_2 = 0.02, \hat{\varphi}_2 = 0.02$.

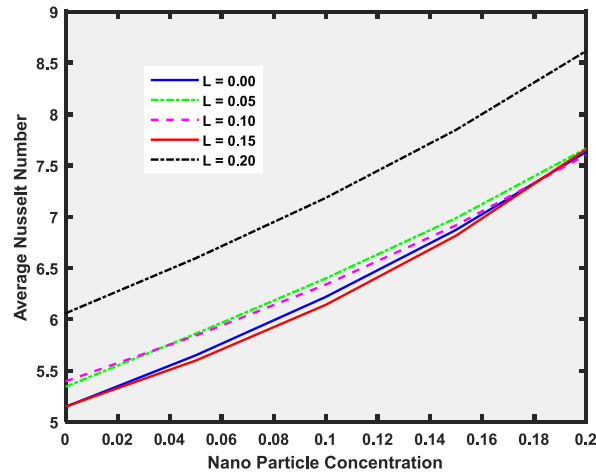


Fig. 15. The Effect of Magnetic Strip Size on the Average Nu with fixed $Mn = 15$, $Re = 15$, $L = 0$, $Pr = 6.2$, $Ec = 10^{-5}$, $\hat{\varphi}_1 = 0.05$, $\hat{\varphi}_2 = 0.02$, $\hat{\varphi}_3 = 0.02$.

values, we monitored much difference in our numerical results at $A_1 = A_2 = 50$ and $A_1 = A_2 = 100$. That's why, for the whole present study we have taken $A_1 = A_2 = 50$ unless otherwise stated.

5.8. The role of magnetic field localization

The magnetic strips can be defined as: $(0.2 - L < \xi < 0.3 + L, 0.7 - L < \xi < 0.8 + L, 0 < \eta < 1)$ and $(0.2 - L < \eta < 0.3 + L, 0.7 - L < \eta < 0.8 + L, 0 < \xi < 1)$. This indicates that the strips have a constant width size of 0.2 units when $L = 0$. The Nusselt number reduces first and then climbs as the value of L increases (i.e., the strip becomes wider). Likewise, when the values of $\hat{\varphi}_1$, $\hat{\varphi}_2$ and $\hat{\varphi}_3$ are larger, the Nu is more sensitive to nanomaterial concentration (See Fig. 15).

6. Concluding remarks

We study the vortex generation and heat transfer enhancement of tri-hybrid nanofluids in a lid-driven cavity under the effect of localized magnetic fields. This is a novel and important research topic that is underexplored in the literature. We used the ADI technique which is efficient, accurate, and stable for complex problems with multiple nanoparticles and magnetic fields. We examined and explained the effects of parameters like Reynolds number, volume fraction, and magnetic field intensity. Based on the results of this study, the following main findings can be summarized:

- Without a magnetic field, almost two identical vortices form symmetrically around the upper and lower lids of the enclosure. The magnetic sources stretch this vortex until it splits into two smaller and weaker vortices (in the lower and upper half of the cavity) that rotate clockwise or counterclockwise.
- The flow experiences various forces from the magnetic fields of the vertical and horizontal strips, which interact with the external force and generate more vortices that rotate in different directions.
- Without a magnetic force, the flow field has mostly red isotherms, indicating higher temperatures. The isotherms are also denser near the top and bottom walls. The magnetic force disrupts any linear temperature distribution in the cavity. The flow creates new vortices that blend fluids with varying temperatures, disrupting the thermal pattern in the enclosure.
- The magnetic field covering the whole flow field does not affect the flow and temperature distributions much. But the localized magnetic field intensity creates new vortices and removes the primary vortices.
- Skin Friction (CfRe) is affected by two parameters in the same qualitative way, but slightly different in quantity. The nano nature of the fluid has a minor effect on skin friction. The Nu depends more on $\hat{\varphi}_1$ than on $\hat{\varphi}_2$ and $\hat{\varphi}_3$ because of the physical features of the nanoparticles. The localized magnetic field does not always change Nu consistently. There may be an optimal width of the magnetic corridor for the Nu.
- The magnetic field strength has increased both the CfRe and the Nu by up to 46% and 100%, respectively. The Reynolds number affects the Nu significantly but not the CfRe.
- The nanoparticles increased both Nu and CfRe, but differently for different types. Silver (Ag) had the highest increase in both (55% and 110%), showing a strong link between the nanofluid's thermal and fluid properties. Alumina Al_2O_3 and Titanium Dioxide (TiO_2) had lower increases in both (33% and 25% for Nu, 13% and 9% for CfRe), showing a weaker link between the nanofluid's properties.
- The average Nu is enhanced more by tri-hybrid nanofluid (Ag, Al_2O_3 , and TiO_2) than by simple nanofluid with Ag, Al_2O_3 , or TiO_2 particles.

- The Nu varies with the strip width (L), it decreases at first and then increases as the strip widened. It also responds more strongly to the nanoparticle concentration when $\hat{\varphi}_1$, $\hat{\varphi}_2$ and $\hat{\varphi}_3$ are higher.

Ethical approval and consent for publication

This study did not involve any human or animal subjects and did not require ethical approval. The authors consent to the publication of this manuscript in Case Studies in Thermal Engineering.

Declaration of competing interest

The authors declare that they have no conflict of interest.

We declare that we have no conflict of interest.

Data availability

Data will be made available on request.

References

- [1] N. Abdullah, et al., Numerical computations of biomagnetic fluid flow in a lid-driven cavity, *CFD Lett.* 12 (4) (2020) 43–53.
- [2] A. Hajesfandiari, G.F. Dargush, A.R. Hadjesfandiari, Size-dependent fluid dynamics with application to lid-driven cavity flow, *J. Non-Newtonian Fluid Mech.* 223 (2015) 98–115.
- [3] S. Biswas, J.C. Kalita, Topology of corner vortices in the lid-driven cavity flow: 2D vis a vis 3D, *Arch. Appl. Mech.* 90 (2020) 2201–2216.
- [4] S. Ahmad, et al., Role of localized magnetic field in vortex generation in tri-hybrid nanofluid flow: a numerical approach, *Nanotechnol. Rev.* 12 (1) (2023), 20220561.
- [5] S. Ahmad, et al., Vortex generation due to multiple localized magnetic fields in the hybrid nanofluid flow—A numerical investigation, *Heliyon* 22 (2023).
- [6] K. Ali, et al., On the interaction between the external magnetic field and nanofluid inside a vertical square duct, *AIP Adv.* 5 (10) (2015).
- [7] K. Ali, et al., Molecular interaction and magnetic dipole effects on fully developed nanofluid flowing via a vertical duct applying finite volume methodology, *Symmetry* 14 (10) (2022) 2007.
- [8] S.U. Choi, J.A. Eastman, Argonne national lab. (ANL), argonne, IL (United States), Enhancing thermal conductivity of fluids with nanoparticles 41 (1995).
- [9] A. Kumar, et al., Analysis of forced convective nanofluid flow through a wavy channel with linearly varying amplitude at the entrance, *Int. J. Numer. Methods Heat Fluid Flow* 65 (2022) (ahead-of-print).
- [10] H. Dey, et al., Numerical investigation of thermo-hydraulic features of viscoplastic flow in wavy channels, *Int. Commun. Heat Mass Tran.* 143 (2023), 106715.
- [11] S.K. Mehta, S. Pati, Thermo-hydraulic and entropy generation analysis for magnetohydrodynamic pressure driven flow of nanofluid through an asymmetric wavy channel, *Int. J. Numer. Methods Heat Fluid Flow* 31 (4) (2021) 1190–1213.
- [12] S. Jayakumar, M. Sreekanth, Numerical investigation of fluid flow and heat transfer in an electrical machine cooling system using nanofluids, in: *IOP Conference Series: Earth and Environmental Science*, IOP Publishing, 2020.
- [13] N. Biswas, et al., A narrative loom of hybrid nanofluid-filled wavy walled tilted porous enclosure imposing a partially active magnetic field, *Int. J. Mech. Sci.* 217 (2022), 107028.
- [14] S.K. Mehta, S. Pati, Analysis of hydrothermal performance for laminar forced convective flow through a wavy channel with porous blocks, *Int. J. Numer. Methods Heat Fluid Flow* 33 (6) (2023) 2128–2152.
- [15] Ahmad, S., et al., Localized Magnetic Fields and Their Effects on Heat Transfer Enhancement and Vortices Generation in Tri-hybrid Nanofluids: A Novel Investigation. Available at SSRN 4499073.
- [16] V. Rajesh, M. Sheremet, Natural convection of ternary hybrid nanofluid in a differential-heated enclosure with non-uniform heating wall, *Micromachines* 14 (5) (2023) 1049.
- [17] K. Shigeno, M. Li, H. Fujimori, Development of novel temperature-stable Al₂O₃-TiO₂-based dielectric ceramics featuring superior thermal conductivity for LTCC applications, *J. Eur. Ceram. Soc.* 41 (1) (2021) 376–386.
- [18] A.M. Elsayed, et al., Preparation of hexagonal nanoporous Al₂O₃/TiO₂/TiN as a novel photodetector with high efficiency, *Sci. Rep.* 11 (1) (2021) 17572.
- [19] S. Zarei, et al., Fabrication of novel 2D Ag-TiO₂/γ-Al₂O₃/Chitosan nano-composite photocatalyst toward enhanced photocatalytic reduction of nitrate, *Int. J. Biol. Macromol.* 145 (2020) 926–935.
- [20] D.L. Northrup, et al., Novel technologies for emission reduction complement conservation agriculture to achieve negative emissions from row-crop production, *Proc. Natl. Acad. Sci. USA* 118 (28) (2021), e2022666118.
- [21] J. Xu, et al., A novel deposition mechanism of Au on Ag nanostructures involving galvanic replacement and reduction reactions, *Chem. Commun.* 57 (67) (2021) 8332–8335.
- [22] M. Khan, et al., Biogenic synthesis of palladium nanoparticles using *Pulicaria glutinosa* extract and their catalytic activity towards the Suzuki coupling reaction, *Dalton Trans.* 43 (24) (2014) 9026–9031.
- [23] M. Khan, et al., Green synthesis of silver nanoparticles mediated by *Pulicaria glutinosa* extract, *Int. J. Nanomed.* (2013) 1507–1516.
- [24] M. Khan, et al., Graphene based metal and metal oxide nanocomposites: synthesis, properties and their applications, *J. Mater. Chem. A* 3 (37) (2015) 18753–18808.
- [25] J.C. Maxwell, *A Treatise on Electricity and Magnetism*, vol. 1, Clarendon Press, Oxford, 1873.
- [26] S. Choi, Z. Zhang, W. Yu, *FE lockwood, EA Grulke*. Anomalous thermal conductivity in nano tube suspension, *Appl. Phys. Lett.* 79 (2001) 2252–2254.
- [27] D.K. Mandal, et al., Nanofluidic thermal-fluid transport in a split-driven porous system working under a magnetic environment, *Int. J. Numer. Methods Heat Fluid Flow* 32 (7) (2022) 2543–2569.
- [28] T. Heindel, S. Ramadhyani, F. Incropera, *Laminar Natural Convection in a Discretely Heated Cavity: I—Assessment of Three-Dimensional Effects*, 1995.
- [29] T.J. Heindel, F. Incropera, S. Ramadhyani, *Laminar Natural Convection in a Discretely Heated Cavity: II—Comparisons of Experimental and Theoretical Results*, 1995.
- [30] T. Heindel, S. Ramadhyani, F. Incropera, Conjugate natural convection from an array of discrete heat sources: part 1—two-and three-dimensional model validation, *Int. J. Heat Fluid Flow* 16 (6) (1995) 501–510.
- [31] T. Heindel, F. Incropera, S. Ramadhyani, Conjugate natural convection from an array of discrete heat sources: part 2—a numerical parametric study, *Int. J. Heat Fluid Flow* 16 (6) (1995) 511–518.
- [32] M. Sankar, J. Park, Y. Do, Natural convection in vertical annuli with discrete heat sources, *Numer. Heat Tran., Part A: Applications* 59 (8) (2011) 594–615.
- [33] A. Müftüoğlu, E. Bilgen, Natural convection in an open square cavity with discrete heaters at their optimized positions, *Int. J. Therm. Sci.* 47 (4) (2008) 369–377.
- [34] G. Nardini, M. Paroncini, Heat transfer experiment on natural convection in a square cavity with discrete sources, *Heat Mass Tran.* 48 (2012) 1855–1865.
- [35] M. Saglam, B. Sarper, O. Aydin, Natural convection in an enclosure with a pair of discrete heat sources, *J. Thermophys. Heat Tran.* 33 (1) (2019) 234–245.

- [36] D.K. Mandal, et al., Role of surface undulation during mixed bioconvective nanofluid flow in porous media in presence of oxytactic bacteria and magnetic fields, *Int. J. Mech. Sci.* 211 (2021), 106778.
- [37] W.L. Hosch, Navier-Stokes equation, URL, <https://www.britannica.com/science/Navier-Stokes-equation>, 2018. (Accessed 20 April 2018).
- [38] F. Talebi, A.H. Mahmoudi, M. Shahi, Numerical study of mixed convection flow in a square lid-driven cavity utilizing nanofluid, *Int. Commun. Heat Mass Tran.* 37 (1) (2010) 79–90.
- [39] V.C. Loukopoulos, E.E. Tzirtzilakis, Biomagnetic channel flow in spatially varying magnetic field, *Int. J. Eng. Sci.* 42 (5–6) (2004) 571–590.
- [40] K. Ali, et al., Insights into the thermal attributes of sodium alginate (NaC₆H₇O₆) based nanofluids in a three-dimensional rotating frame: a comparative case study, *Case Stud. Therm. Eng.* (2023), 103211.
- [41] K. Ali, et al., Impact of magnetic field localization on the vortex generation in hybrid nanofluid flow, *J. Therm. Anal. Calorim.* 56 (2023).
- [42] Y. Kai, et al., A case study of different magnetic strength fields and thermal energy effects in vortex generation of Ag-TiO₂ hybrid nanofluid flow, *Case Stud. Therm. Eng.* (2023), 103115.
- [43] Y. Kai, et al., Thermal case study and generated vortices by dipole magnetic field in hybridized nanofluid flowing: alternating direction implicit solution, *Results Phys.* 49 (2023), 106464.
- [44] N. Acharya, S. Maity, P.K. Kundu, Framing the hydrothermal features of magnetized TiO₂-CoFe₂O₄ water-based steady hybrid nanofluid flow over a radiative revolving disk, *Multidiscip. Model. Mater. Struct.* 134 (2019).
- [45] S. Ahmad, K. Ali, M. Ashraf, MHD flow of Cu-Al₂O₃/water hybrid nanofluid through a porous media, *J. Porous Media* 24 (7) (2021).
- [46] R. Ayub, et al., Numerical assessment of dipole interaction with the single-phase nanofluid flow in an enclosure: a pseudo-transient approach, *Materials* 15 (8) (2022) 2761.
- [47] S. Ahmad, et al., Numerical study of Lorentz force interaction with microstructure in channel flow, *Energies* 14 (14) (2021) 4286.
- [48] S. Ahmad, J. Cai, K. Ali, Prediction of new vortices in single-phase nanofluid due to dipole interaction, *J. Therm. Anal. Calorim.* (2020) 1–15.
- [49] A. Yasmin, K. Ali, M. Ashraf, MHD Casson nanofluid flow in a square enclosure with non-uniform heating using the Brinkman model, *The European Physical Journal Plus* 136 (2) (2021) 1–14.
- [50] T. Shih, C. Tan, B. Hwang, Effects of grid staggering on numerical schemes, *Int. J. Numer. Methods Fluid.* 9 (2) (1989) 193–212.
- [51] C.L. Chen, et al., Lattice Boltzmann simulation for mixed convection of nanofluids in a square enclosure, *Appl. Math. Model.* 39 (8) (2015) 2436–2451.
- [52] G.D. Davis, Natural-Convection of Air in a square cavity - a bench-mark numerical-solution, *Int. J. Numer. Methods Fluid.* 3 (3) (1983) 249–264.